Title

WNTinib is a multi-kinase inhibitor with specificity against β-catenin mutant hepatocellular carcinoma

Permalink

https://escholarship.org/uc/item/5s84b10z

Journal

Nature Cancer, 4(8)

ISSN

2662-1347

Authors

Rialdi, Alex

Duffy, Mary

Scopton, Alex P

et al.

Publication Date

2023-08-01

DOI

10.1038/s43018-023-00609-9

Copyright Information

Peer reviewed

WNTinib is a multi-kinase inhibitor with specificity against β-catenin mutant hepatocellular carcinoma

Alex Rialdi[1,2,3,4,19], **Mary Duffy**[1,5,19], **Alex P. Scopton**[1,19], **Frank Fonseca**[4,1,5], **Julia Nanyi Zhao**[4,3,2,1,5], **Megan Schwarz**[4,3,2,1,5], **Pedro Molina-Sanchez**[2,3,6], **Slim Mzoughi**[1,2,4], **Elisa Arceci**[4,2,1,5], **Jordi Abril-Fornaguera**[5,7], **Austin Meadows**[1,2,4], **Marina Ruiz de Galarreta**[2,3,6], **Denis Torre**[4,3,2,1,5], **Kyna Reyes**[1,2], **Yan Ting Lim**[8], **Felix Rosemann**[2,5], **Zaigham M. Khan**[1], **Kevin Mohammed**[4,1,9], **Xuedi Wang**[10], **Xufen Yu**[1], **Manikandan Lakshmanan**[8], **Ravisankar Rajarethinam**[8], **Soo Yong Tan**[8,11], **Jian Jin**[1], **Augusto Villanueva**[3,12], **Eleftherios Michailidis**[13,14], **Ype P. De Jong**[13,15], **Charles M. Rice**[13], **Ivan Marazzi**[16], **Dan Hasson**[10], **Josep M. Llovet**[3,7,17], **Radoslaw M. Sobota**[8], **Amaia Lujambio**[2,3,5,6,✉], **Ernesto Guccione**[4,3,2,1,6,10,19,✉], **Arvin C. Dar**[1,2,18,19,✉]

[1]Center for Therapeutics Discovery, Department of Oncological Sciences and Pharmacological Sciences, Tisch Cancer Institute, Icahn School of Medicine at Mount Sinai, New York, NY, USA.

[2]Department of Oncological Sciences, Icahn School of Medicine at Mount Sinai, New York, NY, USA.

[3]Liver Cancer Program, Division of Liver Diseases, Department of Medicine, Tisch Cancer Institute, Icahn School of Medicine at Mount Sinai, New York, NY, USA.

[4]Center for OncoGenomics and Innovative Therapeutics, Tisch Cancer Institute, Icahn School of Medicine at Mount Sinai, New York, NY, USA.

[5]Graduate School of Biomedical Sciences, Icahn School of Medicine at Mount Sinai, New York, NY, USA.

[6]The Precision Immunology Institute, Icahn School of Medicine at Mount Sinai, New York, NY, USA.

[7]Translational Research in Hepatic Oncology, Liver Unit, IDIBAPS, Hospital Clinic, University of Barcelona, Barcelona, Spain.

[8]Institute of Molecular and Cell Biology, Agency for Science, Technology and Research, Singapore, Singapore.

[9]Department of Microbiology, Icahn School of Medicine at Mount Sinai, New York, USA.

[10]Bioinformatics for Next Generation Sequencing Shared Resource Facility, Icahn School of Medicine at Mount Sinai, New York, NY, USA.

[11]Yong Loo Lin School of Medicine, National University of Singapore, Singapore, Singapore.

[12]Division of Hematology and Medical Oncology, Tisch Cancer Institute, Icahn School of Medicine at Mount Sinai, New York, NY, USA.

[13]Laboratory of Virology and Infectious Disease, The Rockefeller University, New York, NY, USA.

[14]Laboratory of Biochemical Pharmacology, Department of Pediatrics, School of Medicine, Emory University, Atlanta, GA, USA.

[15]Division of Gastroenterology and Hepatology, Weill Cornell Medicine, New York, NY, USA.

[16]Department of Biological Cancer, University of California Irvine, Orange, CA, USA.

[17]Institució Catalana de Recerca i Estudis Avançats, Barcelona, Spain.

[18]Program in Chemical Biology, Sloan Kettering Institute, Memorial Sloan Kettering Cancer Center, New York, NY, USA.

[19]These authors contributed equally: Alex Rialdi, Mary Duffy, Alex P. Scopton, Ernesto Guccione, Arvin C. Dar.

Abstract

Hepatocellular carcinoma (HCC) is a leading cause of cancer-related deaths worldwide. β-Catenin (*CTNNB1*)-mutated HCC represents 30% of cases of the disease with no precision therapeutics available. Using chemical libraries derived from clinical multi-kinase inhibitor (KI) scaffolds, we screened HCC organoids to identify WNTinib, a KI with exquisite selectivity in *CTNNB1*-mutated human and murine models, including patient samples. Multiomic and target engagement analyses, combined with rescue experiments and in vitro and in vivo efficacy studies, revealed that WNTinib is superior to clinical KIs and inhibits KIT/mitogen-activated protein kinase (MAPK) signaling at multiple nodes. Moreover, we demonstrate that reduced engagement on BRAF and p38α kinases by WNTinib relative to several multi-KIs is necessary to avoid compensatory feedback signaling—providing a durable and selective transcriptional repression of mutant β-catenin/Wnt

targets through nuclear translocation of the EZH2 transcriptional repressor. Our studies uncover a previously unknown mechanism to harness the KIT/MAPK/EZH2 pathway to potently and selectively antagonize *CTNNB1*-mutant HCC with an unprecedented wide therapeutic index.

HCC is the most common form of primary liver cancer, which is currently the fourth leading cause of cancer-related death globally[1,2]. Incidence of this cancer type in the USA has tripled over the last 40 years and, unlike for most cancers, there has been a continued increase in mortality rate[2]. Advanced-stage HCC has a poor prognosis and is treated in the frontline setting with atezolizumab plus bevacizumab[3]. Before this and for over a decade, the mainstay of therapy has been multi-targeted KIs, including the drug sorafenib[2]. Overall response rates to current HCC drugs remain <30% (ref. 2) and personalized therapeutic approaches are lacking, highlighting the need for more effective and targeted therapeutics to treat this heterogeneous cancer[4–6]. Mutations in β-catenin (encoded by *CTNNB1*), which occur in ~30% of cases, are of particular therapeutic interest[2,4–6]. β-Catenin mutant tumors are currently unactionable with precision medicines[2,4–6]. In addition, *CTNNB1* mutations are associated with tumor immune exclusion and inconsistent responses to immunotherapy[3,7–9]. The vast majority of *CTNNB1* mutations inactivate amino-terminal phospho-degron sites, causing stabilization of the protein that enables dysregulated transcriptional activation of several downstream pathways[10]. Given the lack of selective and mutant-specific β-catenin inhibitors or known drug targets without substantial on-target toxicity for the Wnt pathway[10], we sought to identify small molecules that display specific cell toxicity in models of mutant β-catenin. Through chemical genetic screens focused on genetically engineered tumor organoids, we identify a selective antagonist of β-catenin mutant HCC that is effective in vivo and in human-derived model systems. We term this compound WNTinib based on a multiomics strategy that identifies downregulation of oncogenic Wnt signaling via inhibition of KIT/MAPK and downstream activation of EZH2 as the mechanism of action.

Results

WNTinib selectively antagonizes *CTNNB1*-mutated HCC

We recently developed a chemical strategy for the diversification and disease-specific improvement of tool- and US Food and Drug Administration (FDA)-approved multi-KIs[11–13]. Using regorafenib and sorafenib as starting molecules, we developed a library of small molecules that are differentially substituted with hydrocarbon or perfluoroalkane groups at a type II diversity subpocket that is predicted to distinguish kinase targets and anti-targets (Fig. 1a and Extended Data Fig. 1a–e). These small molecules were screened in four tumor organoid models derived from genetically engineered mouse models of HCC (Fig. 1a)[14]. The tumor organoids shared overexpression of *MYC* and possessed unique secondary hits: (1) overexpression of constitutively active 90 β-catenin (*MYC-CTNNB1*), (2) deletion of *Tp53* (*MYC-Tp53*), (3) overexpression of *Tert* (*MYC-Tert*) and (4) deletion of *Pten* (*MYC-Pten*). Screening compounds against these models yielded potent and selective cytotoxicity for WNTinib in the *MYC-CTNNB1* tumor organoids. We additionally identified a structurally related analog (8–50-2), which we used as a control compound for downstream analysis (Fig. 1b and Extended Data Fig. 1f–i). The library was further refined

by performing dose–response curves on tumor organoids and primary human hepatocytes (Fig. 1c). Substitution of length and branch-varying hydrocarbon chains conferred little activity, although activity markedly improved with certain perfluoroalkane substitutions. WNTinib was exemplary for its tumor specificity, as defined by its preferential activity in the *CTNNB1*-driven model compared with hepatocytes. As a caveat to this conclusion, these cells are grown in different culture conditions and have different proliferation rates (Fig. 1c). In addition, we created stable *MYC-CTNNB1* organoids expressing a green fluorescent protein (GFP)-based WNT reporter[15], to assess direct transcriptional inhibition of the pathway. WNTinib was the only compound to downregulate WNT-driven GFP expression. Notably, clinical KIs did not display similar biological specificity nor did they repress the reporter (Fig. 1c). WNTinib's unique specificity was confirmed across a comprehensive set of human HCC cell lines (Fig. 1d), primary patient-derived HCC lines (Fig. 1e) and primary patient-derived HCC organoids (Fig. 1f)—in examples of each, WNTinib induced apoptosis (Extended Data Fig. 1j).

WNTinib represses Wnt pathway transcriptional output

To uncover WNTinib's mechanism of action (MoA) we performed unbiased multiomic experiments in tumor organoids. First, we conducted a phosphoproteomic analysis in WNTinib-sensitive (*MYC-CTNNB1*) and -insensitive (*MYC-Tp53*) tumor organoids at 4 h and 24 h (Fig. 2a, Extended Data Fig. 2a,b and Supplementary Tables 1–4). Although the effects were modest at 4 h post-treatment, after 24 h of treatment, a higher number of phosphoproteins were modulated in the *CTNNB1*-driven model (Fig. 2a). Network enrichment (STRING) for differentially upregulated phosphorylation events identified proteins in the RNA metabolism and splicing pathways, which were redundant in both organoid models. Downregulated phosphorylation events in the *MYC-CTNNB1* organoids were instead unique and enriched for proteins involved in transcription and chromatin organization (Fig. 2a and Extended Data Fig. 2c,d). A computational analysis to assess global signaling event perturbations by WNTinib yielded two main results: (1) WNTinib was predicted to modulate kinases belonging to WNT and MAPK signaling pathways, which was observed in both the *MYC-CTNNB1* and the *MYC-Tp53* organoids; and (2) the WNTinib-modulated substrates of these kinases differed between organoid models and, in the *MYC-CTNNB1* organoids, the phosphorylation of substrates involved in the epigenetic regulation of gene expression was uniquely enriched (for example, EZH2 and ARID1A) (Extended Data Fig. 2e,f). These results strongly linked WNTinib's MoA to chromatin biology. To test this hypothesis, we conducted RNA-sequencing (RNA-seq) in *MYC-CTNNB1* and *MYC-Tp53* organoids treated with WNTinib for 1 h, 24 h or 7 d to detect downstream transcriptional changes. Differential gene expression analyses revealed two meaningful results: (1) WNTinib-mediated transcriptional regulation was divergent between the two models and (2) downregulated genes in the *MYC-CTNNB1* model were enriched for Wnt signaling, development and pluripotency and evident mainly at 7 d post-treatment, consistent with an epigenetic-mediated repression timeline (Fig. 2b and Extended Data Fig. 3a–d). Gene set enrichment analysis (GSEA) revealed a strong and specific correlation between downregulated genes in the *MYC-CTNNB1* organoids and transcriptional bivalency (genes with H3K4me3 and H3K27me3) regulated by the polycomb repressive complex 2 (PRC2) (Supplementary Tables 5–10). Consistent with this result,

WNTinib treatment for 7 d in *MYC-CTNNB1* organoids upregulated the trimethylation of lysine 27 on histone H3 (H3K27me3) at the promoters of repressed genes, many of which belong to Wnt and multicellular organism development pathways as assessed by the CUT&RUN method (Fig. 2c,d and Extended Data Fig. 4b,c)[16]. This upregulation was also validated with chromatin immunoprecipitation (ChIP)–quantitative (q)PCR of H3K27me3 at selected Wnt pathway genes (Extended Data Fig. 4d). Importantly, H3K27me3 did not accumulate at genes not repressed during WNTinib treatment (Extended Data Fig. 4a,c,d).

EZH2 is essential for the activity of WNTinib

Phosphorylation of threonine-367 on EZH2 (pT367 EZH2), a previously described p38 target[17,18], was the most significantly downregulated phosphorylation event under WNTinib treatment spanning the EZH2 protein, which is the catalytic subunit of PRC2 (Extended Data Fig. 5a). This site is also known to control the cellular localization of EZH2, whereby dephosphorylation licenses EZH2 into the nucleus for gene repression[17]. We next used our comprehensive set of HCC models to survey the relationship between *CTNNB1* mutations and pT367 EZH2 levels. Notably, pT367 was detected at baseline in all *CTNNB1*-mutated models (11 out of 11 models) and absent in almost all *CTNNB1* wild-type (WT) models (12 out of 13 models) (Fig. 3a–c and Extended Data Fig. 5b). Strikingly, WNTinib suppressed pT367 in all *CTNNB1*-mutated models, whereas, in contrast, sorafenib induced pT367 in several models, including both *CTNNB1* mutant and WT models. These data suggested a feedback release or possibly paradoxical activation mechanism related to the modulation of EZH2 phosphorylation, which could be induced by sorafenib, but not WNTinib (Fig. 3a–c and Extended Data Fig. 5b). We next evaluated EZH2 localization in multiple *CTNNB1*-mutated models. EZH2 localized to both the cytoplasm and the nucleus—the ratio of such was model dependent. Importantly, baseline pT367 was confined to the cytoplasm (Fig. 3d and Extended Data Fig. 5c,d). On WNTinib treatment, pT367 EZH2 in the cytoplasm was ablated (compare lane 3 with lane 1: pT367 blot), which coincided with an increase in nuclear partitioning of EZH2 (compare lane 6 with 4 and lane 9 with 7: total EZH2 blot) (Fig. 3d and Extended Data Fig. 5c,d). In comparison, sorafenib did not impact phosphorylation or nuclear:cytoplasmic ratios of EZH2 (compare lane 2 with 1: pT367 blot; compare lane 5 with 4 and lane 8 with 7: total EZH2 blot). These nuclear fractionations were validated via immunofluorescence in the *CTNNB1*-mutant primary model 23129 (Fig. 3e). These experiments demonstrate that WNTinib treatment leads to dephosphorylation of pT367, which in turn induces an increase in nuclear EZH2 and a commensurate increase in H3K27me3 deposition and transcriptional repression—in particular, at known Wnt targets (Fig. 2b–d). Furthermore, these experiments demonstrate how WNTinib and sorafenib are mechanistically distinct and further suggested that EZH2 may be essential (albeit without direct physical interaction) for WNTinib's MoA.

We tested the requirement for EZH2 with respect to WNTinib action using two orthogonal methods: (1) genetic depletion of EZH2 (via clustered regularly interspace short palindromic repeats (CRISPR) and short hairpin (sh)RNA) and (2) pharmacological inactivation of EZH2 (via an EZH2 catalytic inhibitor and a degrader). In (1), *MYC-CTNNB1* organoids were transduced with two independent small guide (sg) RNAs targeting *Ezh2* and the response to WNTinib was measured. WNTinib, but not sorafenib, activity was markedly reduced

in organoids lacking EZH2 (Fig. 3f), supporting WNTinib specifically requiring EZH2 for activity. Moreover, in shRNA-transduced organoids, WNTinib activity was reduced and proportional to EZH2 depletion efficiency (Extended Data Fig. 5e). In (2), we used the EZH2 degrader MS1943 or inhibitor GSK343 in combination with WNTinib to further assess the importance of EZH2 on WNTinib activity[19,20]. Consistent with genetic depletion experiments, degradation or inhibition of EZH2 antagonized the activity of WNTinib but did not alter the dose-dependent activity of sorafenib in *MYC-CTNNB1* organoids (Fig. 3g,h and Extended Data Fig. 5f). Importantly, neither small molecule (MS1943 or GSK343) dampened the expression of the WNT reporter, but both rescued the suppressive activity of WNTinib (Extended Data Fig. 5g). Last, we evaluated three putative PRC2 targets (*Jun*, *Wnt16* and *Lef1*) and two nontargets (*Axin2* and *Gapdh*) to examine cooperation between WNTinib and EZH2 at the transcriptional level. *MYC-CTNNB1* organoids depleted for EZH2 and treated with WNTinib generated substantial rescue in the expression of PRC2 targets, which did not occur with either nontargets or sorafenib treatment (Extended Data Fig. 5h). Together, these data demonstrate that WNTinib requires EZH2 for the selective inhibition of Wnt targets in β-catenin mutant HCC.

WNTinib's unique polypharmacology regulates the EZH2–WNT axis

To characterize directly interacting proteins of WNTinib, we first assessed kinome selectivity profiles by in vitro kinase assays. WNTinib maintained potent inhibition against several of the proposed key targets of sorafenib and regorafenib, including KIT, platelet-derived growth factor receptor (PDGFR)α/β, vascular endothelial growth factor receptor (VEGFR)1/2, RET and FLT3 (Supplementary Tables 11–15 and Extended Data Fig. 6a–e); however, WNTinib was generally less promiscuous than the parental compounds based on kinome-wide selectivity scores[21]. To verify WNTinib activity on critical targets directly in vivo, we used bioluminescence resonance energy transfer (NanoBRET)[22] to determine live-cell drug target engagement and the concentration at which a substance exerts half its maximum inhibitory effect (IC_{50}) values. Relative to sorafenib and regorafenib, WNTinib retained similar live-cell IC_{50} values on several receptor tyrosine kinases thought to be critical to the mechanism of sorafenib and regorafenib, including KIT and VEGFR1/2 (Fig. 4a, bottom panel). However, we found that WNTinib was markedly less potent than sorafenib and regorafenib on certain cytoplasmic kinases including BRAF and p38α/β (Fig. 4a, bottom panel). The latter are potentially important in WNT-driven HCCs, given their high expression in the model (Fig. 4a, top panel). Moreover, comparison of WNTinib with the close structural analog 8–50-2 further revealed notable structure–activity relationships (SARs) with notable differences in binding on KIT. This comparative SAR provided the hypothesis and model that we next sought to test—that WNTinib's unique ability to block WNT-driven tumors and specifically modulate pT367 on EZH2 derives from inhibition of KIT in the absence of concurrent and direct engagement on BRAF and p38α/β kinases, where target engagement on the downstream MAPKs elicits release of negative feedback signals that, over time, can override upstream RTK inhibition (Fig. 4b).

As a test of the model with respect to the modulation of KIT/MAPK/EZH2 signaling, we compared our analogs with several benchmark compounds targeting KIT (axitinib), BRAF (vemurafenib) and p38α/β (PH-797804), and conducted an extended time course

in *MYC-CTNNB1* organoids to assess inhibition and potential feedback reactivation. This approach revealed that: (1) both sorafenib and regorafenib dampen phosphorylation of KIT, MEK, p38, ATF2 and EZH2 at early timepoints but succumb to release of feedback signals by 24 h (compare lanes 1–4 with 5–8 or 9–12); (2) 8–50-2 does not affect any pathway signals (compare lanes 1–4 with 13–16); (3) p38α/β inhibition using PH-797804 initially blocks pT367 EZH2, but, by 24 h, returns to baseline levels (compare lanes 1–4 with 21–24); (4) BRAF inhibition using vemurafenib elicits very strong rebound signaling on pT367 EZH2 (compare lanes 1–4 with 25–28); and, last, (5) KIT inhibition using axitinib suppresses, but does not ablate, pT367 EZH2 for up to 48 h (compare lanes 1–4 with 29–32) (Fig. 5a). In contrast, the inhibition dynamics by WNTinib were unique and involved: (1) slightly delayed (relative to sorafenib and regorafenib) but strong and sustained inhibition of p-KIT and pMEK; (2) delayed partial suppression of p-p38; and (3) delayed but strong and sustained inhibition of pT367 EZH2 (compare lanes 1–4 with 17–20) (Fig. 5a). HEPG2 cells were used to conduct a more granular time-course analysis for WNTinib on pT367 EZH2 inhibition, which revealed dephosphorylation of EZH2 by 8 h, which extended to the end of the analysis at 24 h (Extended Data Fig. 6f). In addition, to validate that late (>24 h) feedback on pT367 EZH2 was not a result of drug inactivation in culture medium, we performed a supernatant transfer experiment in HEPG2 cells whereby, after 48 h of drug treatment on an initial cell culture plate, supernatants were removed and transferred to drug-naive cells for the assessment of pT367 EZH2 modulation at 1 and 24 h. Consistent with the biological phenomenon of rebound signaling[23–25], as opposed to drug inactivation, all drug-containing supernatants phenocopied the modulation on pEZH2 observed when fresh drug was added to cells in Fig. 5a (Extended Data Fig. 6g). Taken together, these results indicate marked differentiation of WNTinib from other small molecules and further support the unique target inhibition profile of WNTinib, relative to clinical compounds such as sorafenib and regorafenib, eliciting sustained pT367 EZH2 suppression.

To further understand WNTinib's MoA, we conducted an in vitro kinase assay using either activated ERK or p38 to assess biochemical activity on a small peptide containing the Thr367 residue. As expected[17], p38 was able to phosphorylate Thr367, but we also observed phosphorylation by ERK (Fig. 5b). In addition, WNTinib did not inhibit this phosphorylation in vitro, which confirms its lack of direct engagement on ERK and p38 kinases (Fig. 5c). Together, these data suggest that both the MAP3K/MKK6/p38 and the BRAF/MEK/ERK axes can contribute to the phosphorylation of Thr367 on EZH2 and that, in vivo, WNTinib operates via an upstream targeting mechanism on RTKs including KIT to elicit downstream inhibition on pT367 EZH2 (Fig. 4b).

We next selected the HEPG2 cell line as a suitable model (high pT367 levels, *CTNNB1* mutant) to assess the contribution of individual targets by introducing a series of mutant kinase constructs. For this, we first transduced HEPG2 cells with either an activated MEK1 (Ser218Asp, Ser222Asp) or MKK6 (Ser207Glu, Thr211Glu) construct and assessed pT367 EZH2 modulation and drug efficacy. The expression of each construct was assessed relative to parental lines to assess on-target pathway rescue (Fig. 5d). Strikingly, WNTinib's ability to suppress pT367 was rescued by both constructs—moderately by MKK6 and fully by MEK1 (Fig. 5d; compare lane 5 with 13 and 21, pT367 blot). Moreover, MKK6 overexpression shifted WNTinib's IC_{50} ~30-fold, whereby MEK overexpression effectively

eliminated WNTinib activity in this cell line (Fig. 5e and Extended Data Fig. 6i). Both MKK6 and MEK1 expression decreased the efficacy of sorafenib and regorafenib, although to a limited extent relative to effects on WNTinib, and this rescue appeared independent of substantial changes to pT367 EZH2 (Fig. 5d,e, compare control lanes 2 and 3 with 10 and 11 and 18 and 19, relative to lane 5 with 13 and 21; Extended Data Fig. 6h,i). In addition, both MEK1 and MKK6 overexpression rescued WNTinib-mediated repression of a WNT reporter (Extended Data Fig. 6j), supporting the observed rescue being mediated by the WNT-pathway signaling.

KIT is a critical target of WNTinib

To assess direct binding, we first docked WNTinib into the AspPheGly-out structure of KIT and, consistent with the experimental data, found a compatible binding pose with the $-C_2F_5$ perfluoroalkane of WNTinib buried in the type II allosteric pocket (Fig. 6a, red circle). Stimulation of *MYC-CTNNB1*, but not *MYC-Tp53*, tumor organoids with the KIT ligand stem cell factor (SCF) enhanced growth kinetics (Fig. 6b). Moreover, only WNTinib and not sorafenib activity was antagonized (combination index (CI) >1) by titration of SCF (Fig. 6c). Consistently, the addition of SCF promoted EZH2 phosphorylation at Thr367 and partially rescued WNTinib-mediated repression of this phosphorylation event (Fig. 6d). To directly assess the individual contribution of KIT to the MoA of WNTinib, we stably transduced HEPG2 cells with a doxycycline-inducible vector expressing an activated double mutant (Val599Asp/Thr670Ile). In the present study, we found that KIT overexpression did not change the basal level of pT367 EZH2, but did fully rescue WNTinib's ability to suppress pT367 (Fig. 6e, lane 5 versus 13) and, similar to MEK1 overexpression, greatly reduced WNTinib's efficacy (Fig. 6f and Extended Data Fig. 7a,b). KIT-transduced cells also rescued WNTinib's suppression of the WNT reporter with a similar magnitude to MEK1-transduced cells (Fig. 6g). We took an orthogonal approach to test the importance of KIT to WNTinib's MoA by knocking down the receptor in *MYC-CTNNB1* and *MYC-Tp53* organoids via shRNA. The *cKit* knockdown led to growth suppression in the *MYC-CTNNB1* model while sparing the *MYC-Tp53* model (Extended Data Fig. 7c). In addition, loss of KIT in the *MYC-CTNNB1* organoids downregulated pT367 EZH2 and commensurately upregulated H3K27me3 (Extended Data Fig. 7d). Last, WNTinib's IC_{50} was largely right shifted (increased from <1 μM to >40 μM) in *cKit* knockdown *MYC-CTNNB1* organoids (Extended Data Fig. 7e). Overall, these results demonstrate the fundamental and essential involvement of KIT in the mechanism of WNTinib.

BRAF and p38 are critical anti-targets of WNTinib

We next evaluated the contributions of both BRAF and p38 to the efficacy of WNTinib. First, we engineered drug-resistant constructs for p38α (Thr106Met) and BRAF (Thr529Asn) by mutating critical gatekeeper threonines that are responsible for drug binding[26,27]. Introduction of these constructs did not change the basal level of pT367 EZH2 nor did they alter WNTinib's ability to suppress the mark (Fig. 7a). In addition, WNTinib's efficacy was largely unchanged (Fig. 7b). However, each allele decreased the efficacy of its corresponding control compound (p38-Thr106Met—PH-797804; BRAF-Thr529Asn— vemurafenib) (Extended Data Fig. 8a,b). Notably, introduction of BRAF-Thr529Asn and, to a lesser extent, p38-Thr106Met improved both sorafenib and regorafenib's ability to

suppress pT367 (Fig. 7a; lane 1 versus 2 and 3 compared with 9 versus 10 and 11 and 17 versus 18 and 19), suggesting that removal of anti-target inhibition (that is, increased active p38 or BRAF signaling) strongly improved pT367 pathway inhibition. These differences in pathway inhibition also correlated with improved efficacy for both sorafenib and regorafenib in the mutant cell line relative to parental controls (Extended Data Fig. 8a,b). Notably, introduction of WT BRAF or p38 kinases did not alter the ability of sorafenib or regorafenib to modulate pT367 EZH2 at an early timepoint (1 h) (Extended Data Fig. 8c).

Titration of either a BRAF (dabrafenib) (Fig. 7c) or a p38α/β inhibitor (SB202190) (Fig. 7d) strongly antagonized WNTinib activity (CI > 1) whereas this was not the case for sorafenib, supporting the notion that reduced inhibition of BRAF and p38α/β relative to the clinical analogs (Fig. 4b) contributes to the unique activity of WNTinib. Mechanistically, combining BRAF and p38α/β inhibitors with WNTinib restored EZH2 phosphorylation at Thr367 (Fig. 7e) and also rescued WNTinib-mediated repression of a WNT reporter (Fig. 7f). In an analogous fashion with our overexpression systems that modulated BRAF targetability or pathway activation, BRAF inhibitor (BRAFi) yielded the highest CI and rescue of pT367 EZH2 in combination with WNTinib. Taken together, our data demonstrate a specific vulnerability in *CTNNB1*-mutated HCC that is dependent on EZH2-mediated repression of WNT targets (Fig. 2). WNTinib exploits this vulnerability via targeting of the RTK KIT and reduced engagement of BRAF and p38α/β anti-targets relative to sorafenib/regorafenib, which uniquely avoids the release of negative feedback signaling on pT367 EZH2 (Fig. 4b). Indeed, HEPG2 cells treated with increasing doses of sorafenib or vemurafenib for 1 h induced paradoxical activation of RAF on the downstream effector pT367 EZH2 at low doses but then suppressed it at high doses (Extended Data Fig. 8d). WNTinib did not elicit paradoxical activation and, instead, generated inhibition of only pT367 EZH2; thus, WNTinib acts as a pure antagonist of pEZH2 whereas other KIs such as sorafenib demonstrate mixed agonist/antagonist activity (Extended Data Fig. 8d).

WNTinib outperforms HCC-approved therapeutics in vivo

To understand WNTinib tolerability in mice, we performed in vivo dose escalation in three strains (Fig. 8a and Extended Data Fig. 9a,b). Mice were dosed daily for 2 weeks, and body weight loss was used as a proxy for systemic toxicity. No mice showed signs of sickness, or evident toxicity in the liver, intestine or kidney (Extended Data Fig. 9c), although some weight loss did occur in a dose-dependent manner. To further tailor the dosing of WNTinib, in vivo pharmacokinetics were performed at a dose of 20 mg kg^{-1}. This approach revealed several physiochemical distinctions of WNTinib relative to sorafenib, including a longer half-life (9.38 h versus 8 h), plasma concentration of 7 μM 24 h after oral dosing and detectable quantities of drug in blood plasma up to 72 h post-dosing (Fig. 8b). Based on these data, we achieved preclinical insight into appropriate dosing of WNTinib. *MYC-CTNNB1* tumor organoids were engrafted into C57BL/6 mice and treatment initiated when the tumor volume reached 100 mm^3. The four FDA-approved kinase inhibitors displayed a spectrum of activity but were not able to induce significant tumor regression (Fig. 8c). WNTinib instead induced significant tumor regression in the most animals, thereby validating our in vitro results (Fig. 8c). *MYC-Tp53* tumor organoids were also engrafted and, in this model, consistent with in vitro data, WNTinib was inactive whereas

lenvatinib, sorafenib and regorafenib had measurable anti-tumor activity (Fig. 8d). These results confirm our in vitro specificity observations and indicate that WNTinib demonstrates in vivo selectivity for *CTNNB1*-mutated HCC. Intriguingly, consistent with sustained on-target KIT inhibition, we observed that mice treated for >3 weeks with WNTinib displayed a unique phenotype of fur depigmentation (Extended Data Fig. 9d)[28]. We next repeated the efficacy experiment, allowing *MYC-CTNNB1* organoids to engraft and grow to 300–400 mm^3 before starting treatment, to better mimic an advanced-stage tumor setting. Once again, WNTinib was superior to the standard-of-care clinical compound (sorafenib) (Fig. 8e). Mechanistically, this correlated with in vivo suppression of WNT-target genes (Fig. 8f), induction of apoptotic genes (Extended Data Fig. 9e) and inhibition of EZH2 T367 phosphorylation (Fig. 8g). We last used an autochthonous *CTNNB1*-driven HCC model, which has been used as a model for resistance to immunotherapy and closely recapitulates the therapeutic efficacy observed in patients[9], to test WNTinib efficacy. Mice were treated with either sorafenib or WNTinib and animals were observed for survival. Sorafenib provided a modest survival benefit of 7.5 d. WNTinib conferred a significant survival benefit, where only 40% of its treatment arm succumbed to death with the remaining animals alive >300 d after the final dosing, suggesting that tumors were completely eliminated in these animals (Fig. 8h). Overall, the in vivo efficacy studies highlight that the unique mechanism and target profile of WNTinib strongly distinguish this compound from multiple clinical KIs. These data further support the development of WNTinib as a precision medicine for β-catenin mutant and Wnt-activated tumors.

Discussion

Our work demonstrates a multidisciplinary approach to the discovery and characterization of personalized therapeutics for HCC. In the present study, we identify WNTinib as a multi-targeted KI with selective efficacy in *CTNNB1*-mutated HCC. A multiomics approach provides insight into this compound's unique MoA, revealing nuclear localization of EZH2 and the commensurate repression of Wnt and pluripotency genes as key to WNTinib.

The primary mechanism leading to Wnt-target gene repression by WNTinib is an increase in H3K27me3, which accumulates with slower kinetics (starting at around 24 h) compared with the fast inhibition of upstream RTKs (that is, KIT)[29–31]. These findings suggest EZH2 'reactivation', by upstream KIT/MAPK inhibition, as a unique vulnerability in the *CTNNB1*-mutant model. EZH2's contribution to HCC biology has been studied using multiple models, although no study has investigated its function, or specifically nuclear reactivation, in mutationally defined settings[32–34]. The selection for cytoplasmic sequestration of phospho-EZH2 appears unique to Wnt-activated tumors; this phenomenon could underlie both the selective vulnerability that we observe on nuclear relocalization of EZH2 and the specificity for β-catenin mutant tumors.

Kinase inhibitors for HCC have historically demonstrated modest efficacy in both preclinical models and patients. Our chemical diversification strategy, starting from sorafenib and regorafenib, uncovered WNTinib as a potent and selective antagonist of *CTNNB1*-mutant HCC, suggesting that nonspecific clinical KIs may represent ideal starting points for new drug development campaigns focused on optimizing target and anti-target profiles. In fact,

sorafenib had been shown to dampen Wnt signaling transiently[35], which supported the use of this compound as a starting point to identify related analogs that could function as durable antagonists of the Wnt pathway through reduced anti-target engagement. Our data suggest that key differentiating activities of WNTinib are the removal of the original intended target (BRAF) and the widely recognized off-targets (p38α/β) of sorafenib and regorafenib[36]. The designation of BRAF and p38α/β as anti-targets in the context of mutant β-catenin signaling were validated through genetic and inhibitor combination experiments. Notably, WNTinib inhibits phosphorylation of p38 and ERK substrates, including EZH2, on a much later timescale than direct-acting p38 or MAPK inhibitors and does not elicit detectable compensatory feedback, which we relate to the highly unique profile of WNTinib. This profile is, to the best of our knowledge, an unprecedented demonstration of a multi-targeted KI that modulates both EZH2 phosphorylation and localization.

Several Wnt pathway inhibitors have failed in clinical development due to toxicity[10]; rather than directly acting on β-catenin, WNTinib acts on KIT to phospho-regulate EZH2 to selectively block transcription of Wnt targets. These data suggest that EZH2 activation could be well tolerated in at least some therapeutic settings. Moreover, our data suggest that EZH2 inactivation through phosphorylation on Thr367 and sequestration in the cytoplasm may be required to open chromatin for oncogenic transcription factors such as mutant β-catenin, in a mechanism distinct from what has been described for noncatalytic EZH2 involvement in transcriptional regulation[37]. Such a model for EZH2 activity would be invisible to conventional target identification strategies based on reverse genetics and could explain why the mechanism we have uncovered in the present study has not been documented previously.

Furthermore, the polypharmacological target profile and mechanism of WNTinib would be challenging to identify using purely genetic approaches; thus, the chemical genetic approach that we have employed may be particularly well suited for complex cancers that may require multi-targeted drugs to identify co-target vulnerabilities. In summary, in the present study, we identify that *CTNNB1*-mutated HCC, which makes up almost a third of human cases, may be actioned with a personalized therapeutic that durably inhibits KIT/MAPK-sustained Wnt signaling by harnessing EZH2 repression of Wnt-targeted transcription. Our study provides the rationale to explore WNTinib in proof-of-concept trials with patients with enriched *CTNNB1*-mutant advanced HCC.

Methods

Hydrodynamic tail-vein injections

Vectors were specifically delivered into hepatocytes by injecting a solution of sterile saline (0.9%) containing 10 μg of transposon vectors (pT3-EF1α-*MYC* (Addgene, catalog no. 92046) and pT3-EF1α-Tert, pT3-N90-*CTNNB1* (Addgene, catalog no. 31785)), 10 μg of CRISPR–Cas9 vectors (px330-sgKmt2c, px330-sgPten) and 2.5 μg of the transposon-encoding vector SB13-Luc, according to each specific condition. A volume equivalent to 10% of mouse body weight was injected through the lateral tail vein using a 3-ml syringe with a 26-gauge needle[14].

Tumor organoid derivation and culturing

Sterile digestion medium (0.125 mg ml^{-1} of collagenase from *Clostridium histolyticum*, 0.125 mg ml^{-1} of dispase II and 0.1 mg ml^{-1} of DNase I in phosphate-buffered saline (PBS)) was used to digest liver tumors (2 h at 37 °C). Digested material was put through a 70-μm strainer and washed with basal medium (10 mM Hepes, 1% penicillin–streptomycin and 1% glutamine in advanced Dulbecco's modified Eagle's medium (DMEM)/F-12). After additional washing, 50,000 cells were embedded in 50 μl of Matrigel (Corning) per well of a 24-well plate. Cells were cultured in murine tumor organoid medium (50 ng ml^{-1} of recombinant human hepatocyte growth factor (HGF), 100 ng ml^{-1} of recombinant human fibroblast growth factor 10 (FGF10), 50 ng ml^{-1} of recombinant mouse epidermal growth factor (EGF), 10 nM recombinant human [Leu^{15}]-Gastrin I, 10 mM nicotinamide, 10% Rspo1-conditioned medium, 1 mM *N*-acetylcysteine and 1:50 B-27 in basal medium) until organoids formed[38]. To passage, organoids were taken out of Matrigel in basal medium, spun down at 300g for 5 min at 4 °C, mechanically broken by passing through a 21-gauge needle, washed in basal medium and plated in Matrigel. Patient-derived organoids were cultured in human tumor organoid medium (5 μM A83–01, 10 μM forskolin, 25 ng ml^{-1} of recombinant human HGF, 100 ng ml^{-1} of recombinant human FGF10, 50 ng ml^{-1} of recombinant human EGF, 10 nM recombinant human [Leu^{15}]-Gastrin I, 10 mM nicotinamide, 10% Rspo1-conditioned medium, 1 mM *N*-acetylcysteine, 1:100 N$_2$ and 1:50 vitamin B-27 supplement (B-27) minus vitamin A, in basal medium) and passaged as above. For all tumor organoids, the medium was changed twice a week and the organoids were split on attainment of dense cultures. Hematoxylin and eosin staining was performed as published[38].

Adherent cell-line culturing

Primary cell lines were derived by the laboratory from patients. SNU182 CRL-2235; SNU475 CRL-2236, SNU398 CRL-2233, Hep3B HB-8064 and HepG2 HB-8065 were obtained from American Type Culture Collection. Li7 cells were obtained from RIKEN BRC (catalog no. RCB1941). HUH7 and HUH6 cells were obtained from CLS (catalog nos. 300156 and 305092). All cell lines were grown in complete RPMI (10% fetal bovine serum (FBS), 1% glutamine and 1% penicillin–streptomycin). The medium was changed twice a week and cells were split on attainment of dense cultures.

Drug toxicity assays

For assays in organoid lines, 96-well plates were first coated with a 50:50 solution of basal medium:Matrigel (35 μl per well), which was polymerized for 15 min at 37 °C. Tumor organoids were taken out of Matrigel, broken and washed. Tumor organoids were seeded at 1,000 cells per well and treated the following day with serial dilutions (in the case of IC$_{50}$ curves) or single doses (in the case of the initial screen) of drugs in technical triplicate. Final dimethyl sulfoxide (DMSO) concentrations were kept <0.5%. For adherent lines, cells were seeded at 5,000 cells per well in uncoated 96-well plates. Murine passaged human primary hepatocytes (mpPHHs) were isolated as published and seeded at 40,000 cells per well in collagen-coated 96-well plates[39]. Viability was measured 3 d post-drug administration with either luminescence from CellTiter-Glo or fluorescence from resazurin. Viability data were

analyzed by normalizing individual drug-treated well values to DMSO-treated wells. For the measurement of caspase activity, CaspaseGLO 3/7 was used (Promega).

TOP-GFP Wnt reporter screen

TOP-GFP (Addgene, catalog no. 35489) was used. Cells stably expressing TOP-GFP were generated following lentivirus production and infection methods. After lentivirus infection, a GFP+ cell population was isolated by flow cytometry to establish a stable cell line. For screening WNTinib and analogs in organoids, 5,000 cells per well were plated in black 96-well plates. For screening inhibitors in HEPG2 cells, 50,000 cells per well were plated in 24-well format. Then, 72 h after plating, a baseline fluorescence reading with 472-nm excitation and 512-nm emission was recorded. Fluorescence was again measured 24 h after treatment. Viability was measured by adding resazurin and recording absorbance at 560 and 590 nm. To analyze TOP-GFP reporter output, background fluorescence signal from wells containing medium alone was subtracted and the signal was normalized to the fluorescence reading of DMSO-treated wells. To account for any toxicity with inhibitor treatment, readings were then normalized to the viability readout for each well.

Human primary HCC cell-line generation and genotyping

Sterile digestion medium (1 mg ml^{-1} of collagenase IV in PBS) was used to digest tumor biopsies for 90 min at 37 °C. Digested material was strained though a 70-μm strainer, washed with complete RPMI (20% FBS, 1% glutamine and 1% penicillin–streptomycin) and counted; 100,000 cells were plated on collagen-coated 35-mm plates in primary HCC medium (5 μM A83–01, 10 μM Y-27632 and 40 ng ml^{-1} of recombinant human EGF in complete RPMI). The medium was changed twice a week until the formation of tumor colonies, which were manually picked for further propagation. For *CTNNB1* genotyping, genomic DNA was isolated from cell lines (QIAGEN). The target genomic region was amplified by PCR using primers listed in Supplementary Table 16. PCR was performed using Herculase II Fusion DNA polymerase (Agilent) according to the manufacturer's instructions and 200 ng of genomic DNA as a template. PCR conditions were: 95 °C for 2 min, 95 °C for 0:20 s → 58 °C for 0:20 s → 72 °C for 0:30 s × 34 cycles, 72 °C × 3 min. The PCR product was column purified (QIAGEN) and submitted for MiSeq (Macrogen).

Kinome profiling

WNTinib and 8–50-2's inhibitory profiles were performed using Eurofins' (DiscoverX) KINOMEscan platform. Inhibition trees were visualized using KinMap[40]. For regorafenib and sorafenib, publicly available data were used to visualize inhibition trees[21,41].

Immunofluorescence

Cells were plated at minimal density to achieve precise staining. After drug treatment, the medium was removed and cultures were fixed in 4% paraformaldehyde for 30 min at room temperature. Samples were washed 3× with PBS and permeabilized in PBS (0.5% Triton X-100) for 25 min at room temperature. Blocking was conducted in 2% bovine serum albumin (BSA) for 1 h at room temperature. Primary antibodies (diluted in a 1:1 solution of block:permeabilization solutions) were incubated overnight at 4 °C. Samples

were washed 3× in PBS and secondary antibodies were incubated for 90 min at room temperature. Samples were washed 3× in PBS, DAPI was added and the slides were sealed for imaging. A Zeiss LSM780 confocal system was used for imaging. Antibodies are listed in Supplementary Table 17.

SgRNA design and cloning

SgRNAs for *Ezh2* were designed using the Broad Institute's CRISPick. SgRNAs were cloned into lentiCRISPR v.2 using standard protocols (protocol.io eq2lyn5kpvx9/v1). SgRNA sequences are listed in Supplementary Table 16.

Mass spectrometry, phosphoproteomics

Lysate preparation.—Tumor organoids were grown in 24-well plates and, after drug treatment for 24 h, were collected in Cell Recovery Solution (Corning). Tumor organoids were left to rotate at 4 °C for 1 h to dissolve the Matrigel. Tumor organoids were spun down at 300g and 4 °C for 5 min. Then, 10 million cells were counted, lysed in urea buffer (8 M urea and 50 mM Tris, pH 8.2) for 10 min, sonicated and centrifuged at maximum speed for 10 min at 4 °C. The cleared lysate's concentration was measured using the BCA protein assay. The reduced and alkylated proteins in the lysate were digested overnight with LysC (Wako), followed by another overnight digestion with trypsin (Promega) at the enzyme:protein ratio of 1:25 (mg). Tryptic digestion was stopped with 1% trifluoroacetic acid (TFA) and the digested peptides were desalted using a HLB 6cc cartridge (Waters). The cartridge was conditioned with 1 ml of 100% acetonitrile (ACN), followed by 1 ml of 0.5% acetic acid, and samples were loaded on to the cartridge. The cartridge was washed with 1 ml of 0.5% acetic acid and eluted with 1 ml of 65% ACN in 0.5% acetic acid. The elution was performed once more by reloading the eluate into the cartridge. Phosphoenrichment was performed with the Titansphere (TiO$_2$) method. Input control from the desalted eluate was collected for analysis before enrichment and the remaining eluate was brought to a final concentration of 40% ACN and 6% TFA. Samples were sequentially incubated with 2 mg of Titansphere (GL Sciences) per 1 mg of peptide twice, and the beads were loaded on to C8 Stage-Tips (3M). The beads were washed with 10% ACN, 40% ACN and 60% ACN, all with 6% TFA, and eluted sequentially with 5% ammonia water and 10% ammonia water with 25% ACN. Phosphoenriched eluates were desalted, labeled with TMT6plex (Thermo Fisher Scientific) in 100 mM tetraethylammonium bromide (Sigma-Aldrich) and quenched with 1 M NH$_4$HCO$_2$ (Sigma-Aldrich). The pooled labeled samples were desalted and fractionated with high pH C18 10-μm resin with an increasing concentration of ACN (14%, 18%, 22%, 24%, 27%, 32% and 60%).

Mass spectrometry.—Analysis was performed using the Easy nLC1000 (Thermo Fisher Scientific) chromatography system coupled with Orbitrap (OT) Fusion (Thermo Fisher Scientific). Each sample was separated into 90-min gradients (0.1% formic acid (FA, 99.9% ACN with 0.1% FA) using 50 cm × 75 μm ID Easy-Spray column (C18, 2-μm particles). The following acquisition parameters were applied: data-dependent mode in a speed mode: 3-s cycle, OT–mass spectrometry (MS) resolution 60K, 4×10^5 ions, OT–tandem MS (MS/MS) 7.5K, automatic gain control target of 5×10^4 and higher-energy C-trap dissociation fragmentation at 40% collision energy, isolation window 1 *m/z*.

Data processing.—Peak lists were generated in Proteome Discoverer 2.3 software using Mascot with forward/decoy mouse Uniprot database searches and the following parameters: precursor mass tolerance MS 20 p.p.m., MS/MS 0.06 Da, three missed cleavages, static modifications: carbamidomethyl (C), TMT6plex, variable modifications: acetyl (N-terminal protein), deamidated (NQ), oxidation (M) and phospho (STY), with two levels of false discovery rate (FDR): strict = FDR 1%; medium = FDR 5%.

Computational analysis.—Quantified protein abundances were imported into the R environment to facilitate data analysis and visualization (https://www.R-project.org). Only proteins with at least two quantifying peptide counts were used for downstream analysis. This filtering was not applied to individual site data. Phospho-sites with blank values in both replicates were filtered out; the remaining blank sites were imputed with tail-based imputation function from PhosR (v.1.1.4).

Total phosphoproteins and sites were normalized by first adjusting the summed abundance in each sample to be the same as the averaged value from all the samples, followed by variance stabilization normalization. Differentially phosphorylated sites were identified by Limma (v.3.52.0). Phosphoproteins significantly modulated by WNTinib ($P < 0.05$; $\log_2$(fold-change) $> 1, < -1$) were used to perform a STRING interactome analysis with parameters: highest confidence interaction score and three K-Means clusters. Phosphoproteins belonging to individual clusters were used for a gProfiler analysis to identify enriched reactome pathways, which also identified leading phosphoproteins. To compute kinase–substrate relationships, missing values in raw data were imputed with PhosR (for data available in at least one replicate per condition)[42]. Sites were median centered, with additional normalization to subtract the effect of nonchanging phosphorylated sites. Ratios of samples treated with WNTinib against DMSO were taken for combined kinase–substrate score calculation. Ratios were further filtered based on $P_{adj} < 0.05$ (analysis of variance (ANOVA) test) to identify the top kinases responsible for phosphorylation sites. All phosphoproteomic data files are submitted to JPOST Repository with the identifier (JPST001111; PXID: PXD024958; reviewer access key 1167).

RNA-seq

RNA preparation.—Tumor organoids were grown in 24-well plates and, after drug treatment, were collected in TRIzol. RNA was extracted using standard procedures and quality was assessed with a bioanalyzer. Libraries were built using the PerkinElmer NextFlex Rapid Directional RNA-Seq Kit 2.0 and sequenced with a NovaSeq 6000 (SE75).

Computational analysis.—QC has been performed using FastQC (v.0.11.8). Adapter sequences were removed with Trim Galore! (v.0.6.5) (quality threshold of 20). GRCm38.p6 was used as a reference genome (GENCODE release 25). STAR aligner (v.2.7.5b) was used to perform alignment. Salmon (v.1.2.1) was used to obtain gene-level read counts for all libraries. QC requirements necessitated >50% uniquely mapped reads (>20 million for each library). Gene-level read counts were used to perform the differential expression analyses using the DESeq2 (v.1.28.1) R package. Inactive genes were filtered as having fewer than five reads in total across all samples. Genes with a q value <0.05 (P value adjusted according

to the Benjamini–Hochberg multiple-comparison adjustment) and $\log_2$(fold-change) >0.5 and <−0.5 were included in the following analysis. The GSEA for functional enrichment was performed using the clusterProfiler R package (v.3.16.0) and gProfiler. Between-sample normalization was performed using the variance stabilizing transformation of the DESeq2 package. The 1,000 most variable genes are used to perform principal component analysis as well as calculating the Euclidean distances between each sample. All RNA-seq data files are submitted to the National Center for Biotechnology Information's Gene Expression Omnibus (GEO) database (http://www.ncbi.nlm.nih.gov/geo) with the following accession nos. (superseries GSE213518; subseries GSE213517; reviewer token: ybefgykivdsvfal).

Quantitative PCR

TRIzol-purified RNA, 1 μg, was used for complementary DNA preparation using the Applied Biosystems High-Capacity cDNA kit. Then, qPCR was performed using BioRad SYBR green master mix on a QuantStudio 5 thermal cycler (Thermo Fisher Scientific). Primer sequences can be found in Supplementary Table 16.

CUT&RUN

Sample preparation.—Tumor organoids were grown in 24-well plates and, after drug treatment for 24 h, were collected in Cell Recovery Solution. Tumor organoids were left to rotate at 4 °C for 1 h to dissolve the Matrigel. Tumor organoids were spun down at 300g and 4 °C for 5 min. For each condition, 100,000 cells were counted and washed with PBS. Nuclei were prepared using Epicypher's CUTANA kit and slowly frozen in nuclear extraction buffer. Samples were thawed and CUT&RUN was performed using Epicypher's CUTANA kit with a H3K27me3 antibody (Supplementary Table 17). Sequencing was performed using a NextSeq 550 (PE75).

Computational analysis.—The quality of the raw FASTQC files was evaluated using FastQC (v.0.11.8) and Trim Galore! (v.0.6.5) was then applied to raw reads to remove adaptor and low-quality reads with a quality threshold of 20. Trimmed reads were aligned to the mouse genome reference GRCm38.p6 (GENCODE release M25) using Bowtie2 (v.2.2.8)[43]. Aligned SAM files were converted to BAM files and were filtered to remove mitochondrial reads using SAMtools (v.1.11)[44]. PCR duplication was removed using Picard (v.2.2.4). Reads per kilobase per million mapped reads (RPKM)-normalized bigWig files were generated from the post-filtering BAM files using the bamcoverage function from Deeptools (v.3.2.1)[45]. H3K27me3 levels are visualized for the genes downregulated by WNTinib in *MYC-CTNNB1* tumor organoids ($n = 3{,}767$) and on another set of unchanged genes ($n = 3{,}767$) sampled from all genes for which expression is not significantly modulated by WNTinib, but which have similar mean expression levels to genes downregulated by WNTinib in *MYC-CTNNB1* tumor organoids. H3K27me3 levels were also examined on the genes from selected pathways. Heatmap and profile plots used to visualize H3K27me3 levels were generated using the deepTools computeMatrix and plotHeatmap functions. The bigWig files were loaded into R (v.4.1.0) using the R package rtracklayer (v.1.54.0) to generate genome browser tracks[46]. H3K27me3 read depths near downregulated Wnt pathway genes and near static housekeeping genes were plotted using R package Gviz (v.1.38.4)[47]. All CUT&RUN data files have been submitted to the

NCBI's GEO database (http://www.ncbi.nlm.nih.gov/geo) with accession nos.: superseries GSE213518; subseries GSE213515; reviewer token: ybefgykivdsvfal.

Western blotting

Tumor organoids were grown in 24-well plates and collected in Cell Recovery Solution after drug treatment. Tumor organoids were left to rotate at 4 °C for 1 h to dissolve the Matrigel. Tumor organoids were spun down at $300g$ and 4° for 5 min. Pellets were lysed in 2× Laemmli buffer (+4% 2-mercaptoethanol) by heating at 95 °C for 10 min, followed by 5 s of sonication. Cell lines were trypsinized and lysed as above. Tumor digests (10^6 cells) were lysed as above. Sodium dodecylsulfate (SDS)–polyacrylamide gel electrophoresis (PAGE) was run using standard procedures. Antibody information can be found in Supplementary Table 17 and Reporting summary.

In vitro kinase assay

Recombinant human active kinase MAPK14 (R&D systems, catalog no. 5477-KS) or ERK1 (Carna Biosciences, catalog no. 04–142) was diluted for a final concentration of 10 nM (25 mM Hepes, 10 mM $MgCl_2$ and 0.5 mg ml^{-1} of BSA). Each kinase was incubated with 10 μM ATP (diluted in 25 mM Tris and 10 mM EDTA) and increasing concentrations (1 nM–1 μM) of the customized peptide EZH2 T367–Biotin (PGGRRR-GRLPNNSSRPSTPTINVLESK–Biotin) at room temperature for 10 min, as previously described[48]. Reactions were stopped by diluting them 1:1 with 2× Laemmli buffer (+4% 2-mercaptoethanol) and heated at 95 °C for 10 min. SDS–PAGE was performed using standard procedures.

Cellular fractionation

Tumor organoids were grown in 24-well plates and collected in Cell Recovery Solution after drug treatment. Tumor organoids were left to rotate at 4 °C for 1 h to dissolve the Matrigel. Tumor organoids were spun down at $300g$ and 4 °C for 5 min, counted and 1 million cells were aliquoted per condition. Cells were spun down again at $500g$ and 4 °C for 5 min in ultra-low attachment, 1.5-ml Eppendorf tubes. Cells were resuspended in 100 μl of lysis buffer 1 (50 mM Hepes-KOH, pH 7.5, 140 mM NaCl, 1 mM EDTA, 10% glycerol, 0.5% NP-40, 0.25% Triton X-100 and 1× protease/phosphatase inhibitors) and agitated at 4 °C for 10 min. Lysate was spun at $1,350g$ and 4 °C for 5 min. The supernatant was saved for the cytoplasmic fraction. The pellet was resuspended in 100 μl of lysis buffer 2 (10 mM Tris-HCl, pH 8.0, 200 mM NaCl, 1 mM EDTA, 0.5 mM (ethylenebis(oxonitrilo))tetra-acetate (EGTA) and 1× protease/phosphatase inhibitors) and agitated at room temperature for 10 min. The supernatant was saved for the nuclear soluble fraction. The pellet was resuspended in 35 μl of lysis buffer 3 (10 mM Tris-HCl, pH 8.0, 100 mM NaCl, 1 mM EDTA, 0.5 mM EGTA, 0.1% sodium deoxycholate, 0.5% N-lauroylsarcosine and 1× protease/phosphatase inhibitors) and agitated at 4 °C for 10 min. Then, a 1:10 volume of 10% Triton X-100 was added to the lysate, which was spun down at $20,000g$ and 4 °C for 10 min. Supernatant was taken for the nuclear insoluble fraction. Lysates were diluted 1:1 with 2× Laemmli buffer (+4% 2-mercaptoethanol) and heated at 95 °C for 10 min followed by 5 s of sonication. SDS–PAGE was performed using standard procedures. The same procedure was used for adherent cell lines.

Mutant kinase cloning

Drug-resistant p38-alpha (Thr106Met) and BRAF (Thr529Asn) and constitutively active cKIT (Val599Asp, Thr670Ile) were made using overlapping primers via site-directed mutagenesis on Addgene constructs 64624, 98322 and 114293, respectively. After PCR amplification and DpnI digestion of the nascent methylated plasmid, bacterial transformation yielded colonies that were picked and sequenced to confirm the desired nucleotide/codon changes. Mutant constructs for MEK1 (Ser218Asp, Ser222Asp) and MKK6 (Ser207Glu, Thr211Glu) were obtained from Addgene—items 64604 and 64625, respectively. HepG2 cells stably expressing mutant kinases were generated following lentivirus production and infection methods. In the case of cKIT-transduced cells, doxycycline was added during selection, withdrawn post-selection for 1 week and added before the experiments per set-up. Heterologous expression of the desired mutants was confirmed by western blotting.

Lentivirus production and infection

For EZH2 and KIT depletion, MISSION shRNA constructs were used (Sigma-Aldrich, TRC2 series). The shRNA sequences can be found in Supplementary Table 16. For *Ezh2* knockout, lentiCRISPR v.2 was used (Addgene, catalog no. 52961). To generate lentivirus, HEK293T cells were placed in antibiotic-free DMEM (Gibco) supplemented with 10% FBS. Lentiviral packaging plasmids (pCMV-VSVG, pCMV- 8.9) and plasmids of interest were transfected into cells using Lipofectamine 3000 (Thermo Fisher Scientific). Virus-containing supernatant was harvested 48 and 72 h after transfection, and viral particles were concentrated with Lenti-X Concentrator according to the manufacturer's instructions (Takara Bio). Lenti-X GoStix Plus was utilized to determine virus titer (Takara Bio). For lentiviral infection of HEPG2 cells, lentivirus was added at a multiplicity of infection (MOI) of 3 along with 8 μg ml^{-1} of Polybrene Infection/Transfection Reagent (EMD Millipore). For MKK6/MEK1/p38a/BRAF lentivirus, puromycin was added at a concentration of 2 μg ml^{-1} 48 h after infection. For cKIT lentivirus, blasticidin was added at a concentration of 10 μg ml^{-1} 48 h after infection. Cells were incubated with antibiotics for 4 d or until all cells in an uninfected control well died. After infection and selection, stable overexpression was confirmed by western blotting. For lentiviral infection of organoids, organoids were collected in Cell Recovery Solution and left to rotate at 4 °C for 1 h to dissolve the Matrigel. Organoids were spun down at 300*g* and 4 °C for 5 min. Organoids were dissociated into single cells with TrypLE (Gibco) by rotating at room temperature for 5 min. After rotation, an equivalent volume of basal medium was added, and cells were centrifuged at 300*g* and 4 °C for 5 min. Cells were resuspended in transduction medium (murine tumor organoid medium + 10 μM Y-27632, 3 μM CHIR99021) and TransDUX MAX (Takara Bio) reagents were added according to the manufacturer's instructions. Cell suspensions were distributed into ultra-low attachment, 24-well plates (Corning), and lentiviruses were added at an MOI of 3. Parafilm-wrapped plates were then spun at 600*g* for 1 h at 32 °C. After centrifugation, cells were incubated at 37 °C for 4–6 h. Infected cells were collected in 15-ml conicals, centrifuged at 300*g* for 5 min at 4 °C and redistributed into new 24-well plates in Matrigel. Organoids were grown in transduction medium and 2 μg ml^{-1} of puromycin was added 48 h after infection for all but TOP-GFP-infected organoids. Organoids were incubated with

puromycin for 4 d or until all organoids in an uninfected control well had died. After infection and selection, stable depletion/knockout was confirmed by western blotting.

NanoBRET

For NanoBRET dose–response experiments, HEK293T cells were transfected with NanoLuc Fusion Vectors according to the Promega NanoBRET TE Intracellular Kinase Assay protocol. After overnight transfection, cells were trypsinized and redistributed on a white 96-well plate (20,000 cells per well). Cells were incubated with 1 μM compatible tracer for each vector and inhibitors at doses ranging from 0.02 μM to 20 μM for 2 h. After drug incubation, plates were equilibrated to room temperature for 15 min and NanoBRET Nano-Glo Substrate and Extracellular NanoLuc Inhibitor were added to the wells. Bioluminescent donor (NanoLuc luciferase) and fluorescent acceptor (tracer) emission were measured on a GloMax plate reader at 450 and 600 nm. The BRET ratio is reported as the acceptor signal divided by the donor signal for each well. The conditions were evaluated in technical triplicates for each experiment and experiments were repeated in biological triplicates.

Mice

C57BL/6J, BALB/c and BALB/c nude female mice aged 6 weeks were obtained from Envigo. All mouse studies were approved by the Icahn School of Medicine at Mount Sinai (ISMMS) Institutional Animal Care and Use Committee (IACUC; protocol no. 2018–0013). Mice were maintained under pathogen-free conditions and food and water were provided freely. All animals were examined before initiation of the studies and were acclimated to the laboratory environment for 1 week before use. Sex was not considered in the study design, because it does not play a notable role in the etiology and molecular landscape of HCC.

In vivo studies

Drug preparation.—Solid stocks of drugs were first dissolved in a 1:1 solution of Kolliphor EL:ethanol (Sigma-Aldrich) and frozen at −80 °C. Drugs were diluted with 4 parts water before oral gavage (200 μl per mouse).

Dose escalation studies.—Mice were randomized into treatment groups and daily oral dosing began 1 week after the mice arrived at ISMMS. Body weight was recorded daily and animals were monitored for any signs of sickness throughout the treatment period.

Allograft studies.—Tumor organoids were grown in 24-well plates, taken out of Matrigel in basal medium, spun down at $300g$ for 5 min at 4 °C, mechanically broken by passing through a 21-gauge needle and counted; 300,000 cells per allograft were prepared in 8 mg ml^{-1} of Matrigel. The 6- to 8-week-old C57BL/6J mice were shaved the day before injection. A $26^{5/8}$-gauge needle was used to implant organoids into the flank in 100 μl of Matrigel. Tumor allografts were measured daily with calipers and, on an average volumetric measurement of 100 mm^3, animals were randomized and drug dosing was started. Drugs were dosed daily at 30 mg kg^{-1} via oral gavage. Tumor allografts were also measured daily. For the *MYC-CTNNB1* advanced model, dosing started on an average volumetric measurement of 350 mm^3. Maximal tumor burden size permitted by Mount Sinai's ethic committee is 2 cm^3, which was not exceeded for any studies. C57BL/6 (6BJ) female animals

aged 6 weeks (purchased from Envigo) were used. No statistical methods were used to predetermine sample sizes, but our sample sizes are similar to those reported in previous publications[9,35]. Depending on the experiment and the experimental arm, 5–11 animals were used per group.

HDTV study.—A sterile 0.9% NaCl solution/plasmid mix was prepared containing DNA: 12 µg of *pT3-EF1a-MYC-IRES-luciferase-OS* (*MYC-lucOS*), 10 µg of *pT3-N90-CTNNB1* (*CTNNB1*) and a 4:1 ratio of transposon:*SB13* transposase-encoding plasmid. A volume equivalent to 10% of mouse body weight was injected through the tail vein using a 3-ml syringe with a 26-gauge needle. Animals were monitored for 6 d and bioluminescent signal from tumors was visualized using an IVIS Spectrum system. Anesthetized mice were imaged 5 min after intraperitoneal injection of 100 mg kg^{-1} of d-luciferin (Thermo Fisher Scientific). IVIS Living Image software was used to quantify luciferase signal, which was normalized by subtracting background signal. Mice were randomized into treatment groups, where each group had an equivalent average luciferase signal. Oral drug treatment began in randomized arms 7 d after plasmid injection. KIs were prepared as stated above and WNTinib and sorafenib were dosed at concentrations of 20 mg kg^{-1} and 30 mg kg^{-1}, respectively. Drugs were administered after a 5 d on:2 d off treatment schedule. Body weights were recorded daily and animals were monitored for signs of sickness, tumor palpability and death. Sick animals were sacrificed according to the ISMMS IACUC guidelines. C57BL/6 (6BJ) female animals aged 6 weeks (purchased from Envigo) were used. No statistical methods were used to predetermine sample sizes, but our sample sizes are similar to those reported in previous publications[9,35].

Pharmacokinetics

All animal experiments were carried out in accordance with ethical guidelines and approved by the IACUC, Biological Resource Center (BRC) A*STAR. BALB/c mice were purchased from InVivos and fed with a standard laboratory diet and freely available distilled water. The animals were kept on a 12-h light:dark cycle at 22 ± 2 °C in individually ventilated caging systems with 50–65% humidity in the BRC A*Star, Singapore. For single-dose oral pharmacokinetic studies, female BALB/c mice ($n = 8$, aged 6–8 weeks) were used. The animals were fasted overnight and administered a single oral dose (20 mg kg^{-1}) of WNTinib as prepared above. Blood samples were collected at predetermined timepoints (0 (pre-dosing), 0.5, 1, 2, 4, 8, 12 and 24 h) through the retro-orbital plexus (using micro-hematocrit capillary tubes) into microvette CB300 K2E tubes. A sparse sampling technique (four mice per timepoint) was adopted during blood collection so that blood loss from each mouse was kept to <10% of the total blood volume. Plasma was harvested by centrifuging the blood using a Sorvall Legend Micro 21R centrifuge (Thermo Fisher Scientific) at 1,000g for 15 min and stored at -80 ± 10 °C until further analysis. Mice were allowed to access feed 2 h post-dosing and freely available water. Pharmacokinetic analysis of these compounds was performed using a Shimadzu UFLC prominence system (equipped with degasser (DGU-20A5), isopump (LC-20AD), autosampler (SIL-20AC HT) and column oven (CTO-20AC)) connected to a Sciex 4000 Q-Trap liquid chromatography–MS/MS with heated electrospray ionization source. The primary stock solution (1.0 mg ml^{-1}) of WNTinib and carbamazepine (internal standard (IS)) was prepared in DMSO and

used for subsequent dilutions. Required secondary and working stocks were prepared from the primary stocks using ACN:water (75:25, v:v) as a diluent for the calibration curve (CC) and QC studies. For the pharmacokinetic analysis, the mouse plasma was mixed with carbamazepine (50 ng ml^{-1}, final concentration) and extraction solvent (70% ACN and 0.1% FA) and shaken for 10 min. After vigorous shaking, the samples were centrifuged at 22,000 g for 20 min and the supernatant was collected. Chromatographic resolution of compound and the IS was achieved by injecting 1–2 μl of the processed sample on a Luna C18 100-Å column (50 × 2.0 mm^2, 5 μm; Phenomenex) maintained at room temperature using a mobile phase consisting of 5 mM ammonium formate (buffered with 0.1% formic acid) and ACN delivered at a flow rate of 0.4 ml min^{-1}. Quantification was carried out using multiple reaction monitoring of the transitions.

Docking

WNTinib was docked into the structure of c-KIT in the DFG-out conformation using coordinates from the Protein Data Bank (PDB accession no. 1T46). Coordinate and restraint files for WNTinib were generated with eLBOW[41]. Docking was performed manually based on the expected type II conformation of WNTinib and then optimized using real-space refinement in Coot[21] and maximum-likelihood protocols in Phenix[42].

Statistics and reproducibility

All experiments were repeated at least two to three times with similar results. Statistics were done in Prism 9 (GraphPad). Data distribution was assumed to be normal, but this was not formally tested. As noted in the figure legends, comparisons between groups were calculated using two-tailed, paired Student's *t*-tests. For comparisons between multiple groups, two-way ANOVA tests were used (*F* and degrees of freedom noted, repeated measure). For survival analyses, log(rank *P*) values were calculated (repeated measure). No statistical method was used to predetermine sample size. No data were excluded from the analyses. Animal experiments were randomized by assigning each animal a number and using a random number generator to assign groups. Mathematically equivalent grouping distributions were confirmed (volumes for allografts; luminescence for hydrodynamic tail vein injection experiments). If equivalence was not achieved, random shuffling was done again. The investigators were not blinded to allocation during the experiments and outcome assessment. Data collection and analysis were not performed blind to the conditions of the experiments.

Extended Data
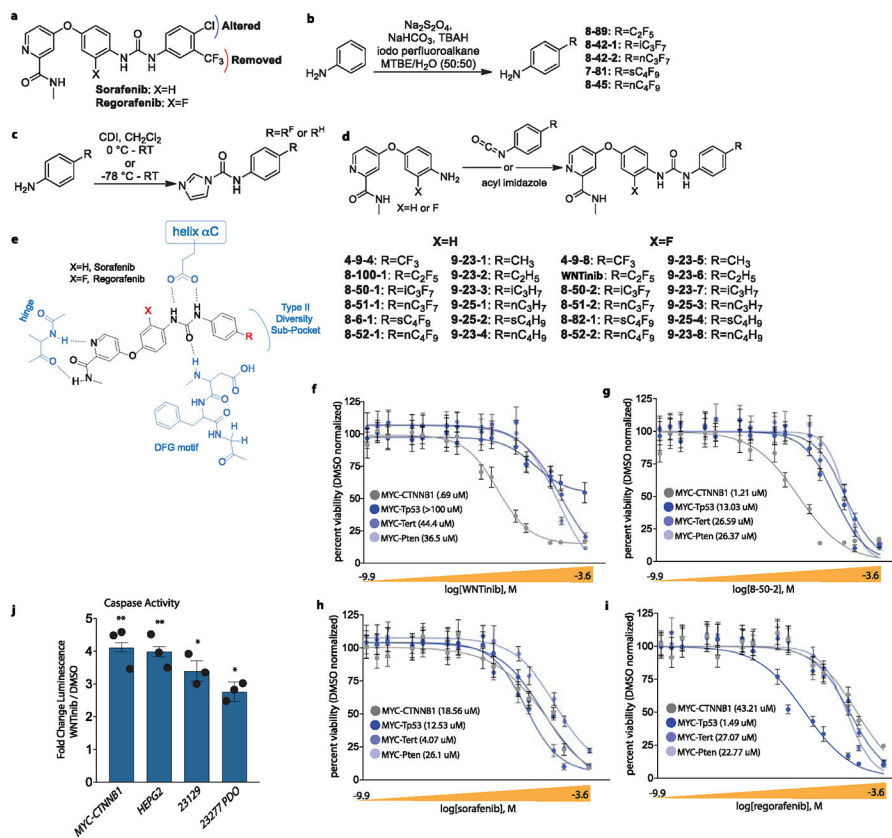
Extended Data Fig. 1 |. Chemical genetic screens in tumor organoids yield WNTinib as a selective antagonist of CTNNB1-mutated HCC.

a, The base structures of sorafenib and regorafenib were used as starting points for kinase inhibitor development. **b**, The required perfluoroalkyl-substituted aniline building blocks were obtained in a single step from aniline. **c**, In cases where isocyanates were not commercially available, the required acyl imidazole intermediates were generated *in situ* from an aniline and *N,N'*-carbonyldiimidazole. **d**, In the final inhibitor generating step, the urea linker component was formed via reaction of a commercially available isocyanate or *in situ* formed acyl imidazole with a core aniline corresponding to sorafenib (X = H) or regorafenib (X = F). **e**, Key interactions and predicted binding pose of sorafenib and regorafenib analogs. Points of diversification are highlighted as X and R, which are specified for each analog in panel d. **f-i**, IC$_{50}$ curves of WNTinib (**f**), 8–50-2 (**g**), sorafenib (**h**), and regorafenib (**i**) in murine HCC organoids used in Fig. 1a. N = 3 independent experiments [mean, SEM]. **j**. Caspase activity in *CTNNB1*-mutant models treated with WNTinib at 1 μM for 3 days. N = 3 independent experiments [mean, SEM]. Extended data associated with Fig. 1.
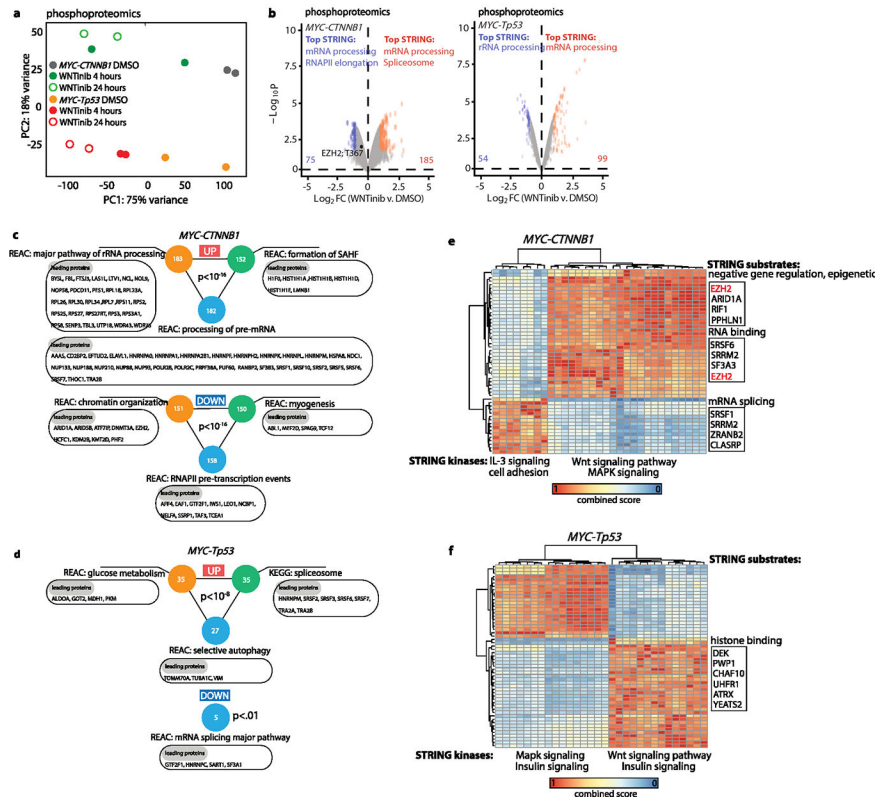
Extended Data Fig. 2 |. WNTinib reduces EZH2 phosphorylation to drive the suppression of essential gene networks in CTNNB1-mutated HCC.

a, Principal component analysis (PCA) of phosphoproteomics displaying *MYC-CTNNB1* and *MYC-Tp53* tumor organoids treated or not with WNTinib for 4 or 24 hours, as related to Fig. 2a. **b**. Volcano plots depicting phosphoproteomic changes elicited by WNTinib in *MYC-CTNNB1* tumor organoids (left) or *MYC-Tp53* tumor organoids (right) as compared to DMSO. Inset: pathway enrichment terms associated with significantly regulated phosphoproteins. WNTinib was used at 1 μM for 4 hours. N = 2 independent experiments. Gene-centered, differentially expressed phosphosites were determined by using estimates of variance-mean dependence with a Benjamini-Hochberg FDR correction. **c-d**, Interaction networks and pathway enrichment for the significantly up and downregulated phosphoproteins in the *MYC-CTNNB1* (**c**) and *MYC-Tp53* (**d**) models treated with WNTinib used at 1 μM for 24 hours. Strength of interactions denoted by STRING *P* value. Proteins driving pathway enrichment shown in boxes. **e-f**, Clustered heatmap of the combined score for kinase-substrate predictions (a higher combined score indicates a stronger kinase-substrate prediction) for the top substrates (y-axis) and kinases (x-axis) modulated by WNTinib in *MYC-CTNNB1* (**e**) and *MYC-Tp53* (**f**) tumor organoids. Pathway enrichment for both kinases and substrates was done using STRING. Substrates driving enrichment shown in boxes; EZH2 highlighted in red. Extended data associated with Fig. 2.
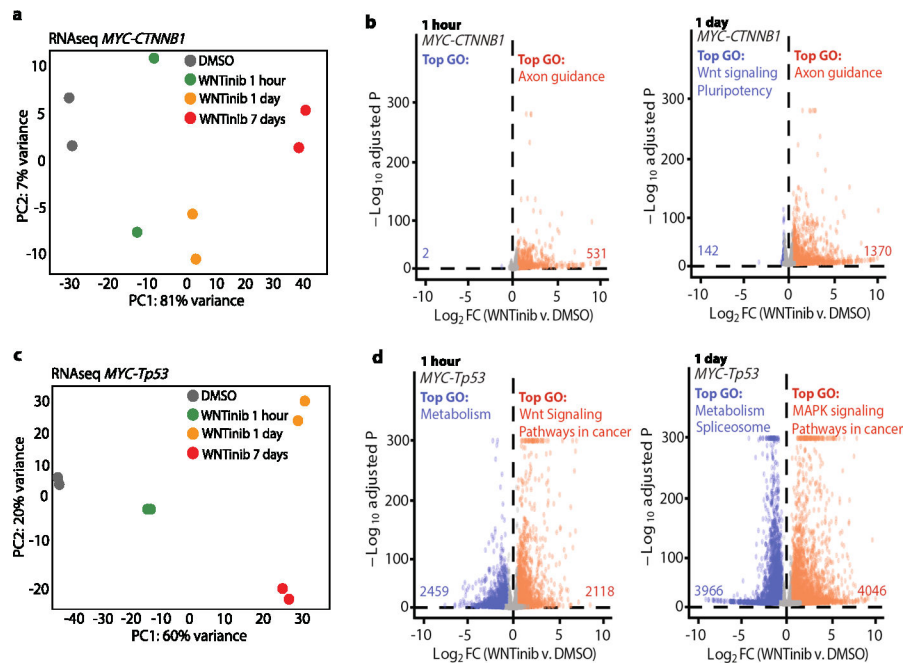
Extended Data Fig. 3 |. WNTinib reduces EZH2 phosphorylation to drive the suppression of essential gene networks in CTNNB1-mutated HCC.
a-b, PCA of transcriptomics (**a**) displaying *MYC-CTNNB1* tumor organoids treated or not with WNTinib for 1 hour, 24 hours, or 7 days, as related to Fig. 2b. N = 2 independent experiments. **b**, Volcano plots depicting transcriptomic changes elicited by WNTinib as related to panel **a**. Inset: pathway enrichment terms associated with significantly regulated transcripts. **c-d**, PCA of transcriptomics (**c**) displaying *MYC-Tp53* tumor organoids treated or not with WNTinib for 1 hour, 24 hours, or 7 days, as related to Fig. 2b. N = 2 independent experiments. **d**, Volcano plots depicting transcriptomic changes elicited by WNTinib as related to panel **c**. Inset: pathway enrichment terms associated with significantly regulated transcripts. For panels **b, d** – differential events were identified using two-sided Wald tests with Benjamini-Hochberg multiple testing corrections. Extended data associated with Fig. 2.
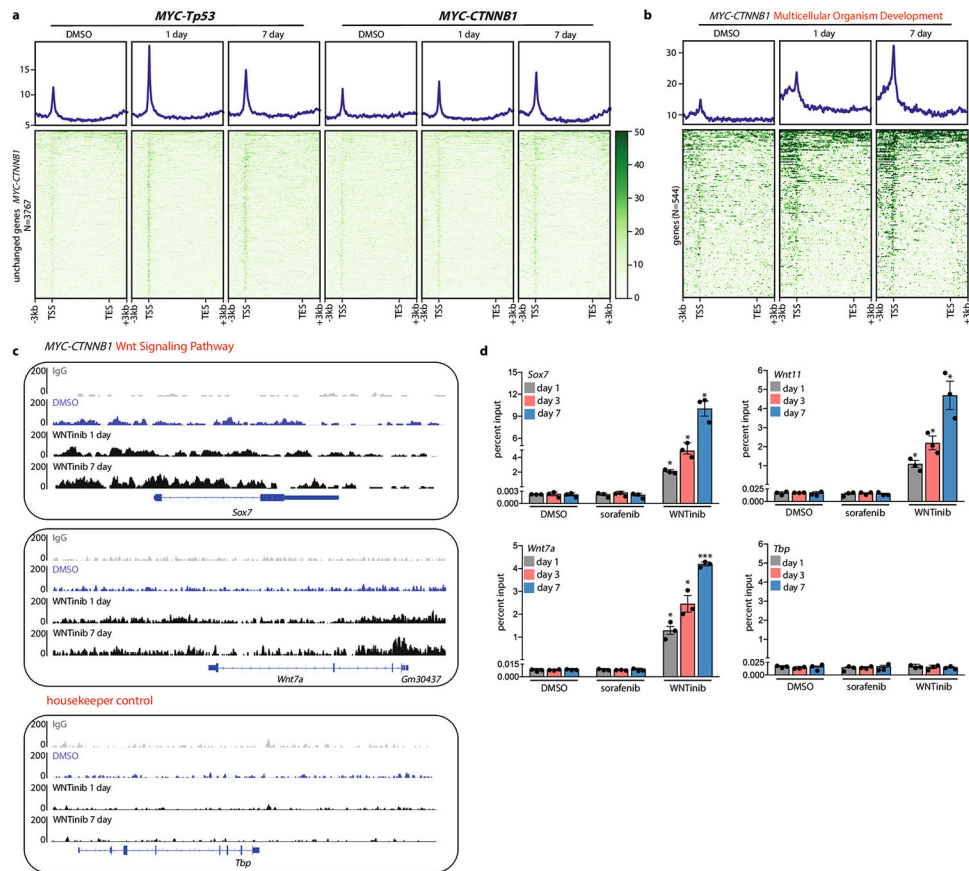
Extended Data Fig. 4 |. WNTinib reduces EZH2 phosphorylation to drive the suppression of essential gene networks in CTNNB1-mutated HCC.

a, Heat maps and average profile plots for *MYC-CTNNB1* tumor organoids (right) or *MYC-Tp53* tumor organoids (left) displaying CUT&RUN H3K27me3 signal around the TSS/TES (+ /− 3 kb) of genes unchanged by WNTinib in the *MYC-CTNNB1* tumor organoids (RNAseq – 7 days; N = 3767). Genes were chosen for similar expression levels to WNTinib-modulated genes. **b**, As in **a**, but displaying H3K27me3 levels at genes belonging to the Multicellular Organism Development Pathway in WNTinib-treated *MYC-CTNNB1* tumor organoids. **c**, Representative genome browser tracks of H3K27me3 levels in WNTinib-treated *MYC-CTNNB1* tumor organoids. Top: examples belong to Wnt Signaling Pathway; Bottom: example of a housekeeping gene. **d**, ChIP-qPCR enrichment of H3K27me3 at the promoters of genes shown in panel **c**. *MYC-CTNNB1* tumor organoids were treated with DMSO, sorafenib (10 μM), or WNTinib (1 μM) for the indicated times. N = 3 independent experiments [mean, SEM]. *P* values; *Sox7* *.00698 (1 day), *.0085 (3 day), *.01045 (7 day); *Wnt11* *.02699 (1 day), *.02624 (3 day), *.02432 (7 day); *Wnt7a* *.01741 (1 day), *.01263 (3 day), ***.00045 (7 day); as calculated with two-tailed paired t-tests. Extended data associated with Fig. 2.
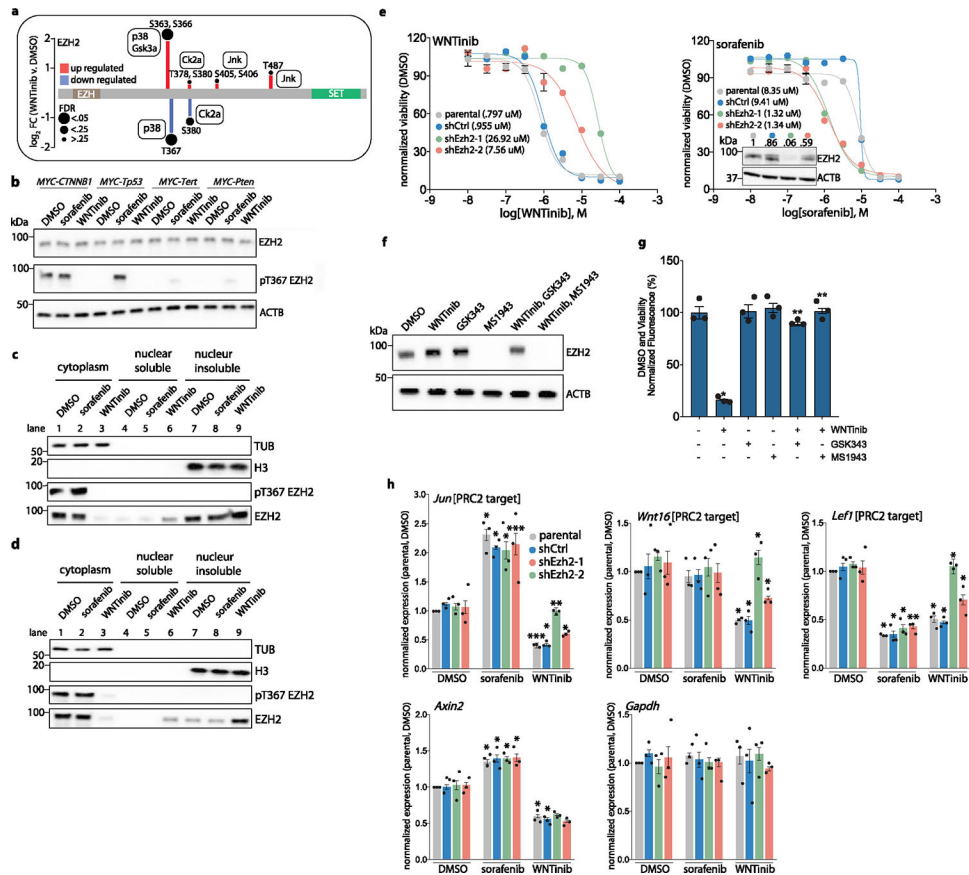
Extended Data Fig. 5 |. WNTinib depends on EZH2 relocalization to chromatin for its activity in CTNNB1-mutated HCC.

a, Schematic of phospho-site regulation of EZH2 by WNTinib in the *MYC-CTNNB1* tumor organoids. Predicted kinases for each site shown in boxes. **b**, Western blot depicting the modulation of pT367 EZH2 by WNTinib (1 μM) or sorafenib (10 μM) in the four tumor organoid models used in Fig. 1a. Tumor organoids were treated for 24 hours. **c-d**, Cytoplasmic and nuclear fractions of total and pT367 EZH2 from *MYC-CTNNB1* organoids (**c**) or HEPG2 cells (**d**) treated with DMSO, sorafenib (10 μM organoids, 5 μM cells), or WNTinib (1 μM organoids, .5 μM cells) for 24 hours. Tubulin and histone H3 used as fractionation controls. **e**, IC$_{50}$ curves for WNTinib (left) or sorafenib (right) in *MYC-CTNNB1* tumor organoids depleted for EZH2 (with two independent shRNA targeting EZH2). Inset: western blot depicting depletion efficiency. N = 3 independent experiments [mean, SEM]. **f**, Western blot depicting total EZH2 degradation as related to Fig. 3g. **g**, WNT reporter expression levels in *MYC-CTNNB1* organoids treated with WNTinib (1 μM), GSK343 (1 μM), or MS1943 (1 μM) alone or in combination. Values obtained from three biological replicates [mean, SEM, n = 3]. Significant differences between groups indicated by asterisks. * $P < .05$, ** $P < .005$, as calculated with two-tailed, paired t-tests. **h**, RNA expression levels of genes in *MYC-CTNNB1* tumor organoids depleted for EZH2 and treated with DMSO, sorafenib (10 μM), or WNTinib (1 μM). Genes are classified as being described PRC2 targets or not. N = 3 independent experiments [mean, SEM]. Significant differences between groups indicated by asterisks. * $P < .05$, ** $P < .005$, *** $P < .0005$ as

calculated with two-tailed, paired t-tests. Exact *P* values listed in source data. Western blot results were independently validated at least two times. Extended data associated with Fig. 3.
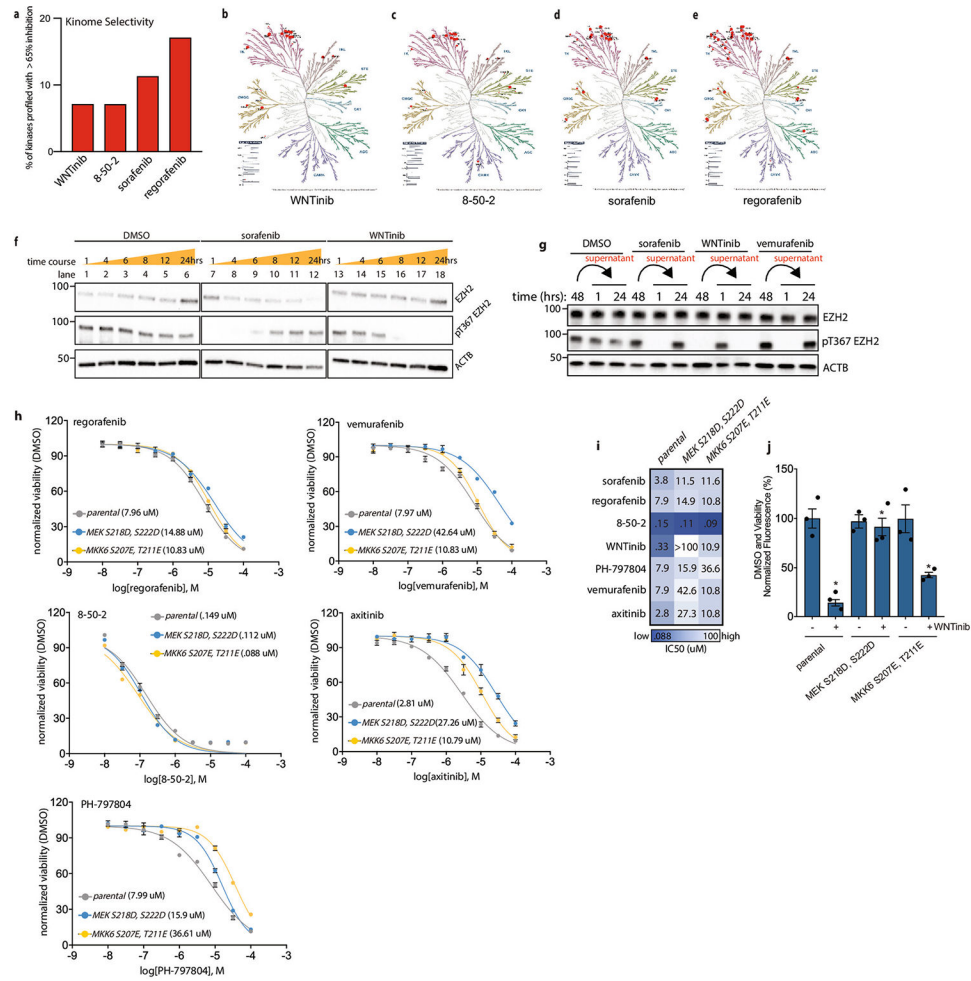
Extended Data Fig. 6 |. WNTinib utilizes unique polypharmacology to regulate the EZH2-WNT axis.

a, Kinome selectivity for sorafenib, regorafenib, 8–50-2, and WNTinib. Y-axis indicates the number of kinases that each compound inhibits at >65%, as profiled using KINOME*scan*. **b-e**, Trees depicting the kinome inhibition profiles of WNTinib (**b**), 8–50-2 (**c**), sorafenib (**d**), and regorafenib (**e**). **f**, Time course (1 to 24 hours) of signaling perturbations on pT367 EZH2. HEPG2 cells were treated with DMSO, sorafenib (5 μM) or WNTinib (.5 μM). Western blot measures endogenous proteins as indicated. **g**, Supernatant transfer experiment in HEPG2 cells. Cells were first treated with DMSO, sorafenib (5 μM), WNTinib (.5 μM), or vemurafenib (10 μM) for 48 hours. Supernatants were harvested and applied to fresh cells for the indicated times and pT367 EZH2 levels were measured. **h**, IC_{50} curves and **i**, Heatmap depicting IC_{50} values associated with each treatment condition in Fig. 5d–e. HEPG2 cells were transduced with constructs encoding constitutively active MEK (S218D, S222D) or MKK6 (S207E, T211E). Parental HEPG2 cells used as control comparison.

Cells were treated for 3 days. Values obtained from three biological replicates [mean, SEM, n = 3]. **j**, WNT reporter expression levels in HEPG2 transduced as in panel **h** and treated or not with WNTinib (.5 μM) for 24 hours. Parental HEPG2 cells used as control comparison. N = 3 independent experiments [mean, SEM]. Significant differences between groups indicated by asterisks. * P< .05, as calculated with two-tailed paired t-tests. P values; *.0291 (*WNTinib*), *.0181 (*MEK WNTinib*), *.0352 (*MKK6 WNTinib*). Western blot results were independently validated at least two times. Extended data associated with Figs. 4 and 5.
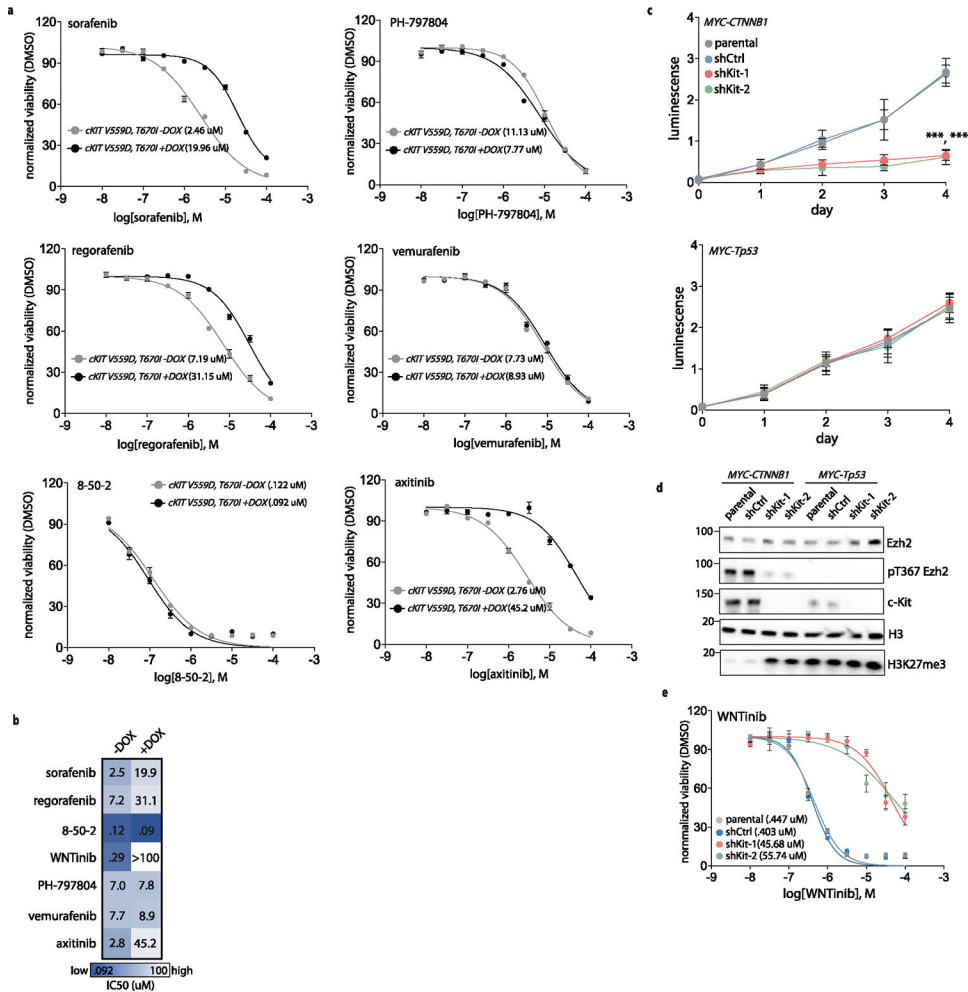
Extended Data Fig. 7 |. KIT is a critical target for WNTinib's MoA.
a, IC$_{50}$ curves and **b**, Heatmap depicting IC$_{50}$ values associated with each treatment condition in Fig. 6e–f. HEPG2 cells were transduced with a doxycycline (DOX)-inducible construct encoding constitutively active cKIT (V559D, T670I). Cells not treated with DOX used as control comparison. Cells were treated for 3 days. Values obtained from three biological replicates [mean, SEM, n = 3]. **c**, Growth curves for *MYC-CTNNB1* tumor organoids (left) or *MYC-Tp53* tumor organoids (right) depleted for KIT using shRNA. Depletion efficiency represented in panel **d**. N = 3 independent experiments [mean, SEM]. Significant differences between curves (as compared to untreated) indicated by asterisks.

*** $P < .0005$, as calculated with a two-way ANOVA with Tukey test for multiple comparisons ($F (4, 20) = 38.99$). **d**, pT367 EZH2 and H3K27me3 modulation in shKIT *MYC-CTNNB1* tumor organoids and *MYC-Tp53* tumor organoids. Western blot measures endogenous proteins as indicated. **e**, IC_{50} curves for WNTinib in *MYC-CTNNB1* tumor organoids depleted for KIT. Organoids were treated for 3 days. N = 3 independent experiments [mean, SEM]. For panel **c**, *P* values; ***<.0001 (*shKit-1, shKit-2*). Extended data associated with Fig. 6.
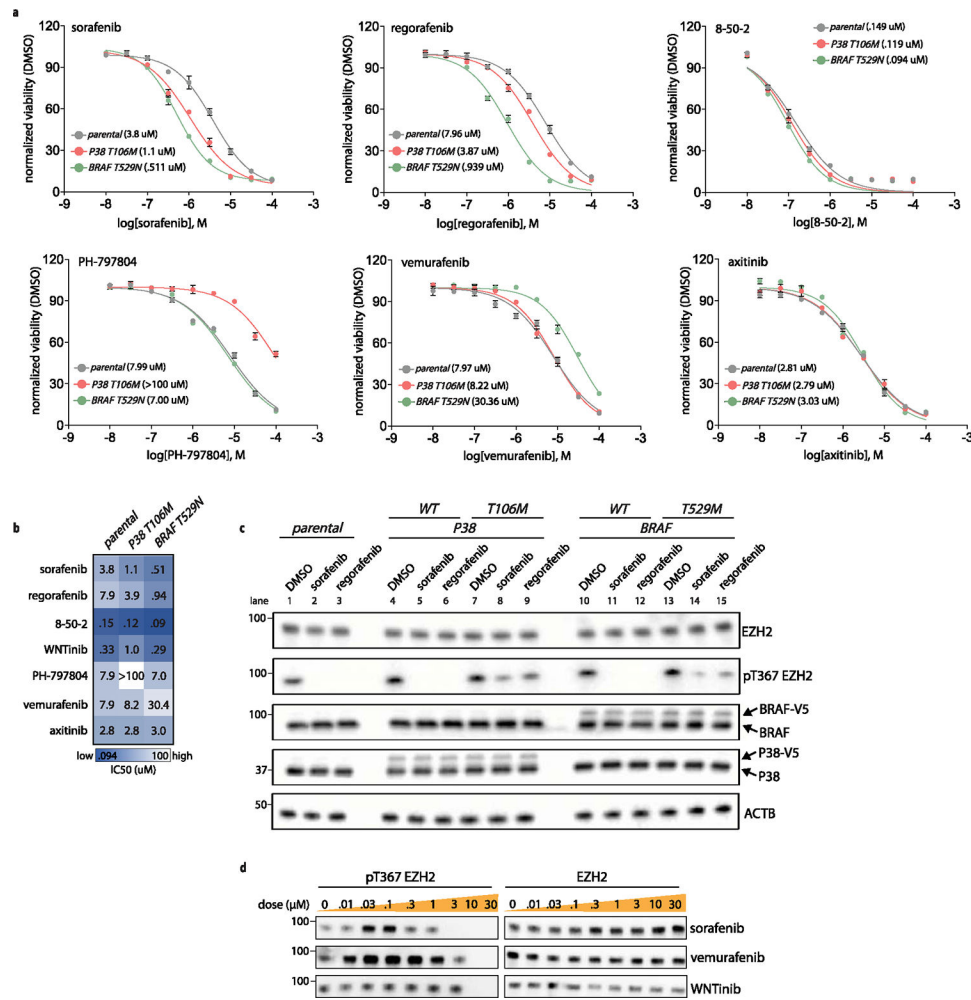
Extended Data Fig. 8 |. BRAF and p38 kinases are critical anti-targets for WNTinib.
a, IC_{50} curves and **b**, Heatmap depicting IC_{50} values associated with each treatment condition in Fig. 7a–b. HEPG2 cells were transduced with constructs encoding drug resistant p38 (T106M) or BRAF (T529N) kinases. Parental HEPG2 cells used as control comparison. Cells were treated for 3 days. N = 3 independent experiments [mean, SEM]. **c**, Total and pT367 EZH2 levels in HEPG2 cells transduced with constructs encoding wildtype or drug resistant p38 (T106M) or BRAF (T529N) kinases. Parental HEPG2 cells used as control comparison. Cells were treated with DMSO, sorafenib (5 μM), or regorafenib (10 μM) for 1 hour. Endogenous antibodies used to assess overexpression of mutant constructs. **d**, Total and pT367 EZH2 levels in HEPG2 cells treated with DMSO, sorafenib, vemurafenib, or

WNTinib at increasing doses (.01 μM to 30 μM) for 1 hour. Western blot results were independently validated at least two times. Extended data associated with Fig. 7.
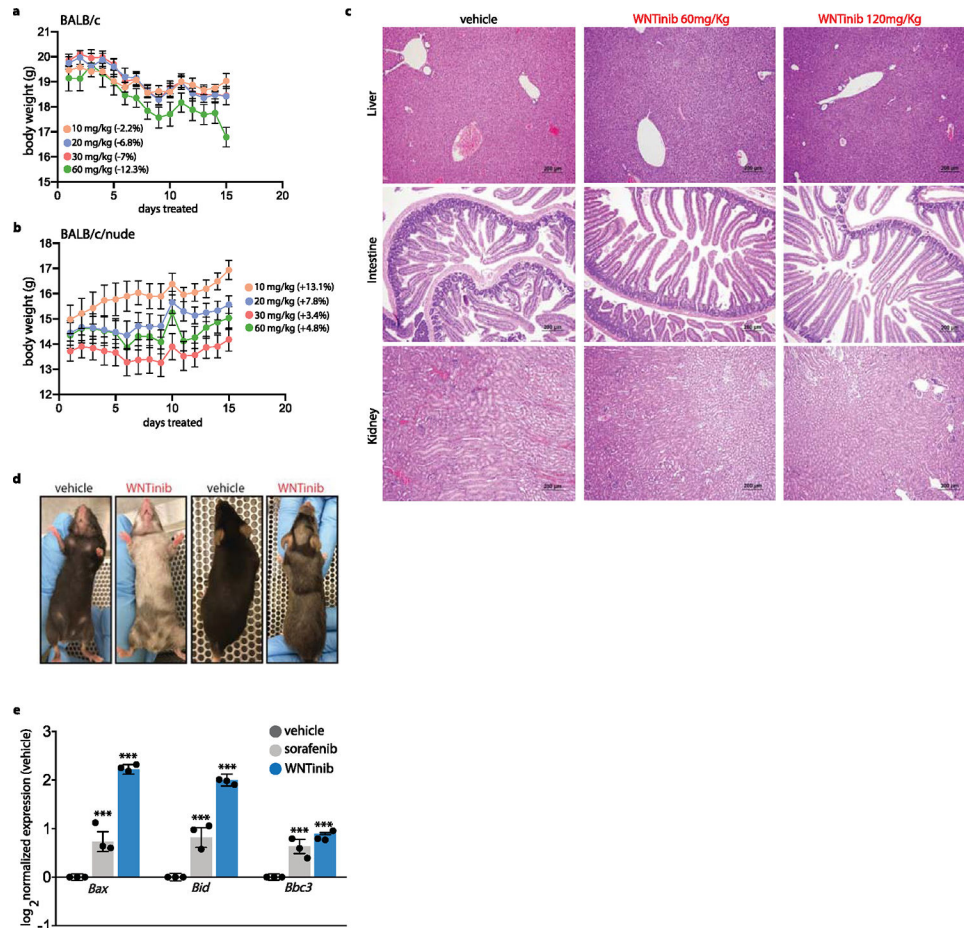
Extended Data Fig. 9 |. WNTinib outperforms clinical compounds across *in vivo* models of HCC.
a-b, Dose escalation of WNTinib in BALB/c mice (**a**) and BALB/c/nude mice (**b**). Animals were dosed every day via oral gavage for 2 weeks. Percentage change in body weight noted in brackets (N = 3 animals per group; mean, SEM). **c**. Histological images (H&E) of liver, small & large intestine, and kidney from BALB/c mice treated with WNTinib at either 60 mg/kg or 120 mg/kg via oral gavage for 14 days. **d**, Images of C57BL/6 J mice treated with either vehicle or WNTinib for extended periods of time. WNTinib-treated animals present mosaic patterns of grey hair. **e**, Quantitative PCR expression of apoptotic genes in tumors derived from mice in panel Fig. 7e (N = 3 per group). *** $P < .0005$, as calculated with two-tailed paired t-tests. Exact *P* values listed in source data. For panel **c**, representative images are shown (n = 3). Extended data associated with Fig. 8.

Supplementary Material

Refer to Web version on PubMed Central for supplementary material.

Acknowledgements

Data availability

All data needed to evaluate the conclusions in the present study are in the paper and/or its supplementary materials. CUT&RUN and RNA-seq data that support the findings of the present study have been deposited in the GEO under accession nos. GSE213518 (subseries GSE213515 and GSE213517). MS data have been deposited in the JPOST Repository with the identifier (JPST001111; PXID: PXD024958). Source data are provided with this paper. All other data supporting the findings of the present study are available from the corresponding author on reasonable request.

References

1. Yang J et al. A global view of hepatocellular carcinoma: trends, risk, prevention and management. Nat. Rev. Gastroenterol. Hepatol. 16, 589–604 (2019). [PubMed: 31439937]

2. Llovet JM et al. Hepatocellular carcinoma. Nat. Rev. Dis. Primers 7, 6 (2021). [PubMed: 33479224]

3. Finn R et al. Atezolizumab plus bevacizumab in unresectable hepatocellular carcinoma. N. Engl. J. Med. 382, 1894–190 (2020). [PubMed: 32402160]

4. Harding J et al. Prospective genotyping of hepatocellular carcinoma: clinical implications of next-generation sequencing for matching patients to targeted and immune therapies. Clin. Cancer Res. 25, 2116–2126 (2018). [PubMed: 30373752]

5. Ally A et al. Comprehensive and integrative genomic characterization of hepatocellular carcinoma. Cell 169, 1327–1341 (2017). [PubMed: 28622513]

6. Hoshida Y et al. Integrative transcriptome analysis reveals common molecular subclasses of human hepatocellular carcinoma. Cancer Res. 69, 7385–7392 (2009). [PubMed: 19723656]

7. Sia D et al. Liver cancer cell of origin, molecular class, and effects on patient prognosis. Gastroenterology 152, 745–761 (2017). [PubMed: 28043904]

8. Bassaganyas L et al. Copy-number alteration burden differentially impacts immune profiles and molecular features of hepatocellular carcinoma. Clin. Cancer Res. 26, 6350–6361 (2020). [PubMed: 32873569]

9. Ruiz de Galarreta M et al. β-Catenin activation promotes immune escape and resistance to anti–PD-1 therapy in hepatocellular carcinoma. Cancer Discov. 9, 1124–1141 (2019). [PubMed: 31186238]

10. Jung YS et al. Wnt signaling in cancer: therapeutic targeting of Wnt signaling beyond β-catenin and the destruction complex. Exp. Mol. Med. 52, 183–191 (2020). [PubMed: 32037398]

11. Dar AC et al. Chemical genetic discovery of targets and anti-targets for cancer polypharmacology. Nature 486, 80–84 (2012). [PubMed: 22678283]

12. Sonoshita M et al. A whole-animal platform to advance a clinical kinase inhibitor into a new disease space. Nat. Chem. Biol. 14, 291–298 (2018). [PubMed: 29355849]

13. Yu JX et al. Phenotype-based screens with conformation-specific inhibitors reveal a p38 gamma and delta as targets for HCC polypharmacology. Mol. Cancer Ther. 18, 1506–1519 (2019). [PubMed: 31213506]

14. Molina-Sanchez P et al. Cooperation between distinct cancer driver genes underlies intertumor heterogeneity in hepatocellular carcinoma. Gastroenterology 159, 2203–2220 (2020). [PubMed: 32814112]

15. Horst D et al. Differential WNT activity in colorectal cancer confers limited tumorigenic potential and is regulated by MAPK signaling. Cancer Res. 72, 1547–1556 (2012). [PubMed: 22318865]

16. Skene PJ & Henikoff S An efficient targeted nuclease strategy for high-resolution mapping of DNA-binding sites. eLife 6, e21856 (2017). [PubMed: 28079019]

17. Anwar T et al. p38-mediated phosphorylation at T367 induces EZH2 cytoplasmic localization to promote breast cancer metastasis. Nat. Commun. 9, 2801 (2018). [PubMed: 30022044]

18. Consalvi S et al. Praja1 E3 ubiquitin ligase promotes skeletal myogenesis through degradation of EZH2 upon p38 activation. Nat. Commun. 8, 13956 (2017). [PubMed: 28067271]

19. Verma SK et al. Identification of potent, selective, cell-active inhibitors of the histone lysine methyltransferase EZH2. ACS Med. Chem. Lett. 3, 1091–1096 (2012). [PubMed: 24900432]

20. Ma A et al. Discovery of a first-in-class EZH2 selective degrader. Nat. Chem. Biol. 16, 214–222 (2020). [PubMed: 31819273]

21. Davis M et al. Comprehensive analysis of kinase inhibitor selectivity. Nat. Biotechnol. 29, 1046–1051 (2011). [PubMed: 22037378]

22. Robers MB et al. Quantifying target occupancy of small molecules within living cells. Annu. Rev. Biochem. 89, 557–581 (2020). [PubMed: 32208767]

23. Lito P et al. Tumor adaptation and resistance to RAF inhibitors. Nat. Med. 19, 1401–1409 (2013). [PubMed: 24202393]

24. Lee S et al. Targeting MAPK signaling in cancer: mechanisms of drug resistance and sensitivity. Int. J. Mol. Sci. 21, 1102 (2020). [PubMed: 32046099]

25. Chandarlapaty S Negative feedback and adaptive resistance to the targeted therapy of cancer. Cancer Discov. 2, 311–319 (2012). [PubMed: 22576208]

26. Lisnock J et al. Molecular basis for p38 protein kinase inhibitor specificity. Biochemistry 38, 3456 (1999). [PubMed: 10079093]

27. Whittaker S et al. Gatekeeper mutations mediate resistance to BRAF-targeted therapies. Sci. Transl. Med. 2, 35ra41 (2010).

28. Moss KG et al. Hair depigmentation is a biological readout for pharmacological inhibition of KIT in mice and humans. J. Pharmacol. Exp. Ther. 2, 476–480 (2003).

29. Ferrari KJ et al. Polycomb-dependent H3K27me1 and H3K27me2 regulate active transcription and enhancer fidelity. Mol. Cell 53, 49–62 (2014). [PubMed: 24289921]

30. Reveron-Gomez N et al. Accurate recycling of parental histones reproduces the histone modification landscape during DNA replication. Mol. Cell 72, 239–249 (2018). [PubMed: 30146316]

31. Oksuz O et al. Capturing the onset of PRC2-mediated repressive domain formation. Mol. Cell 70, 1149–1162 (2018). [PubMed: 29932905]

32. Bugide S et al. Inhibition of enhancer of zeste homolog 2 (EZH2) induces natural killer cell-mediated eradication of hepatocellular carcinoma cells. Proc. Natl Acad. Sci. USA 115, E3509–E3518 (2018). [PubMed: 29581297]

33. Gao SB et al. EZH2 represses target genes through H3K27-dependent and H3K27- independent mechanisms in hepatocellular carcinoma. Mol. Cancer Res. 12, 1388–1397 (2014). [PubMed: 24916103]

34. Xiao G et al. EZH2 negatively regulates PD-L1 expression in hepatocellular carcinoma. J. Immunother. Cancer 7, 300 (2019). [PubMed: 31727135]

35. Lachenmeyer A et al. Wnt-pathway activation in two molecular classes of hepatocellular carcinoma and experimental modulation by sorafenib. Clin. Cancer Res. 18, 4997–5007 (2012). [PubMed: 22811581]

36. Wilhelm SM et al. Preclinical overview of sorafenib, a multikinase inhibitor that targets both Raf and VEGF and PDGF receptor tyrosine kinase signaling. Mol. Cancer Ther. 7, 3129–3140 (2008). [PubMed: 18852116]

37. Jung HY et al. PAF and EZH2 induce Wnt/B-Catenin signaling hyperactivation. Mol. Cell 52, 193–205 (2013). [PubMed: 24055345]

38. Broutier L et al. Culture and establishment of self-renewing human and mouse adult liver and pancreas 3D organoids and their genetic manipulation. Nat. Protoc. 1, 1724–1724 (2016).

39. Michailidis E et al. Expansion, in vivo–ex vivo cycling, and genetic manipulation of primary human hepatocytes. Proc. Natl Acad. Sci. USA 117, 1678–1688 (2020). [PubMed: 31915293]

40. Eid S et al. KinMap: a web-based tool for interactive navigation through human kinome data. BMC Bioinf. 18, 16 (2017).

41. Uitdehaag J et al. Comparison of the cancer gene targeting and biochemical selectivities of all targeted kinase inhibitors approved for clinical use. PLoS ONE 9, e92146 (2014). [PubMed: 24651269]

42. Kim HJ et al. PhosR enables processing and functional analysis of phosphoproteomic data. Cell Rep. 34, 108771 (2021). [PubMed: 33626354]

43. Langmead B & Salzberg SL Fast gapped-read alignment with Bowtie 2. Nat. Methods 9, 357–359 (2012). [PubMed: 22388286]

44. Heng L et al. The sequence alignment/map format and SAMtools. Bioinformatics 25, 2078–2079 (2009). [PubMed: 19505943]

45. Ramirez F et al. deepTools2: a next generation web server for deep-sequencing data analysis. Nucleic Acids Res. 44, W160–W165 (2016). [PubMed: 27079975]

46. Lawrence M et al. rtracklayer: an R package for interfacing with genome browsers. Bioinformatics 25, 1841–1842 (2009). [PubMed: 19468054]

47. Hahne F & Ivanek R Visualizing genomic data using Gviz and Bioconductor. Methods Mol. Biol. 1418, 335–351 (2016). [PubMed: 27008022]

48. Knight ZA et al. A membrane capture assay for lipid kinase activity. Nat. Protoc. 2, 2459–2466 (2007). [PubMed: 17947987]
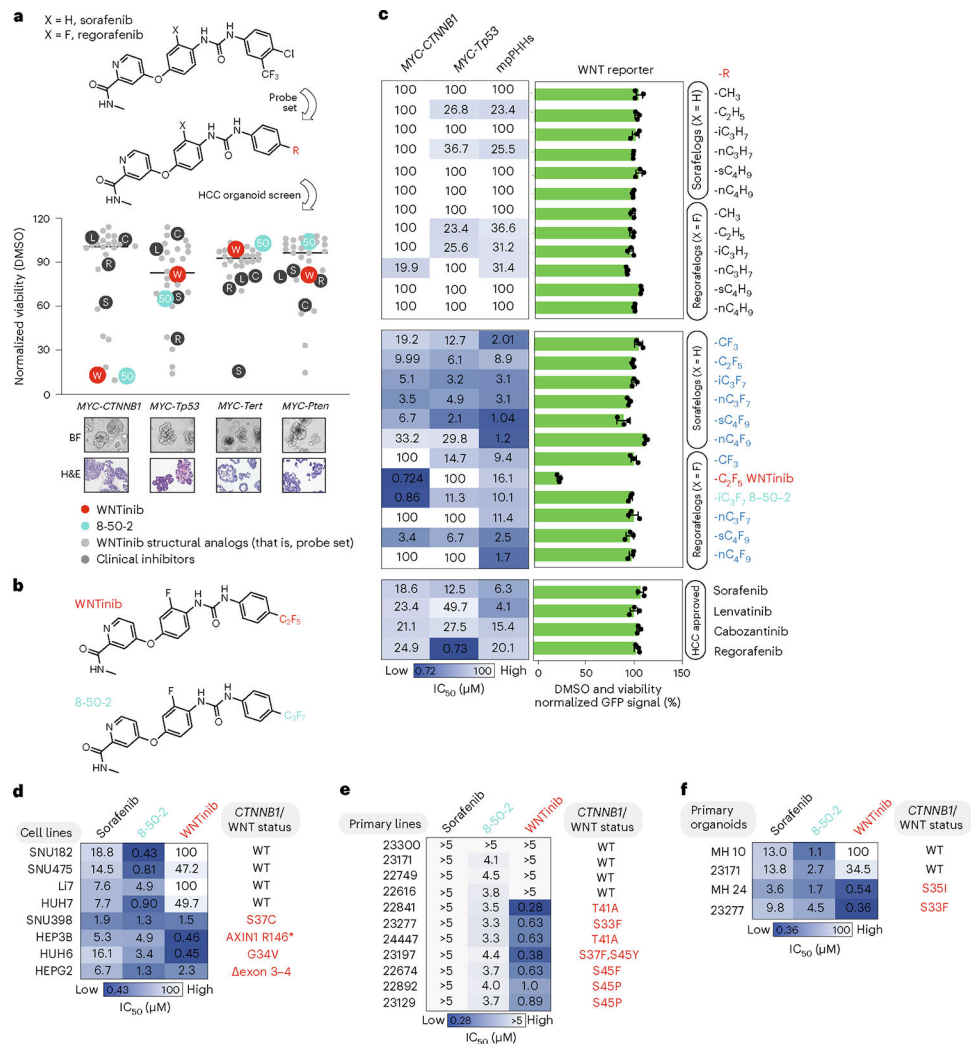
Fig. 1 |. Chemical genetic screens in tumor organoids yield WNTinib as a selective antagonist of *CTNNB1*-mutated HCC.

a, Top, a probe set was derived from sorafenib and regorafenib, with points of diversification highlighted by R, which are specified for each analog in **c**. Bottom, viability of murine HCC organoid models (below: brightfield and histology) treated with the probe set or HCC-approved compounds. The 5-μM activity shown with endpoint viability was measured after 3 d (*n* = 2 independent experiments). Sorafenib, regorafenib, lenvatinib and cabozantinib were denoted by S, R, L and C, respectively. WNTinib and 8–50-2 are highlighted in red and turquoise, respectively. **b**, Chemical structures of WNTinib and 8–50-2. **c**, Left, IC$_{50}$ values for probe set and HCC-approved compounds in *MYC-CTNNB1* tumor organoids, *MYC-Tp53* tumor organoids and mpPHHs (*n* = 2 independent experiments). Right, WNT reporter expression levels in *MYC-CTNNB1* tumor organoids treated with the same compounds (*n* = 3 independent experiments (mean, s.e.m.)). The R column illustrates the cap group diversity of analogs. WNTinib and 8–50-2 are highlighted in red and turquoise, respectively. **d–f**, IC$_{50}$ values for sorafenib, 8–50-2 or WNTinib in human HCC cell lines (**d**), primary human HCC cell lines (**e**) and primary human HCC organoids (**f**). *CTNNB1* or WNT-pathway mutations are noted in the rightmost column (*n* = 3 independent experiments).
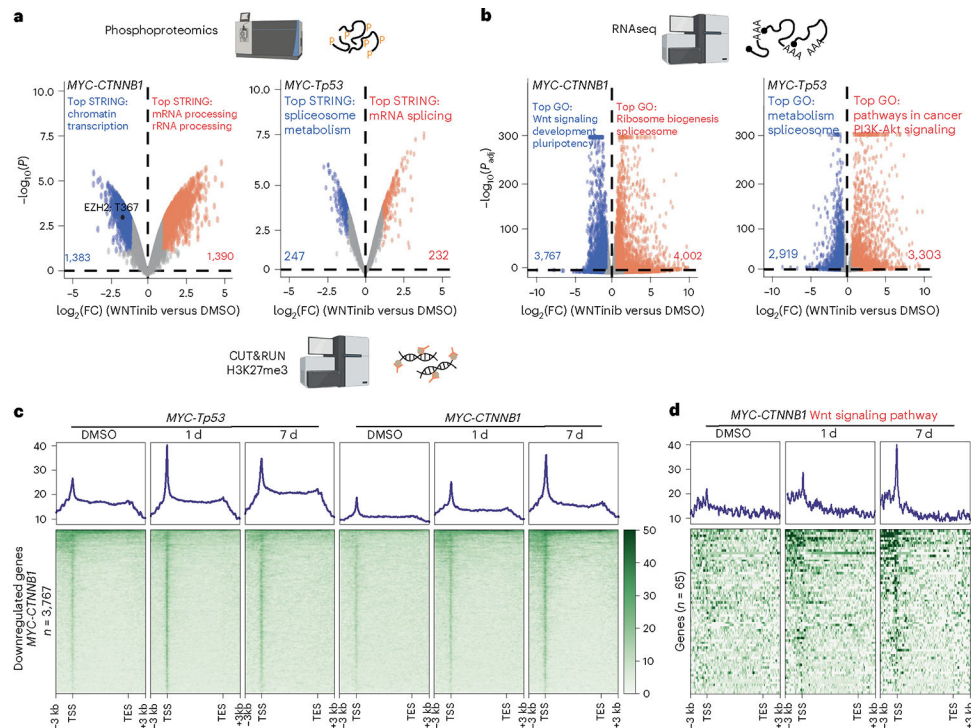
Fig. 2 |. WNTinib reduces EZH2 phosphorylation to drive the suppression of essential gene networks in *CTNNB1*-mutated HCC.

a, Volcano plots depicting phosphoproteomic changes elicited by WNTinib in *MYC-CTNNB1* tumor organoids (left) or *MYC-Tp53* tumor organoids (right) compared with DMSO. Inset, pathway enrichment terms associated with significantly regulated phosphoproteins. WNTinib was dosed at 1 μM for 24 h ($n = 2$ independent experiments). Gene-centered, differentially expressed phospho-sites were determined by using estimates of variance-mean dependence with a Benjamini–Hochberg FDR correction. FC, fold-change. **b**, Volcano plots depicting messenger RNA abundance changes elicited by WNTinib in *MYC-CTNNB1* tumor organoids (left) or *MYC-Tp53* tumor organoids (right) compared with DMSO. Inset, pathway enrichment terms associated with significantly regulated transcripts. WNTinib was dosed at 1 μM for 7 d ($n = 2$ independent experiments). Differential events were identified using two-sided Wald's tests and Benjamini–Hochberg multiple-testing corrections. GO, gene ontology. **c**, Heatmaps and average profile plots for *MYC-CTNNB1* tumor organoids (right) or *MYC-Tp53* tumor organoids (left) displaying CUT&RUN H3K27me3 signal around the transcription start or end site (TSS/TES) (±3 kb) of genes downregulated by WNTinib in the *MYC-CTNNB1* tumor organoids (RNA-seq, 7 d, **b**; $n = 3,767$ genes). **d**, As in **c**, but displaying H3K27me3 levels at genes belonging to the Wnt signaling pathway in WNTinib-treated *MYC-CTNNB1* tumor organoids.
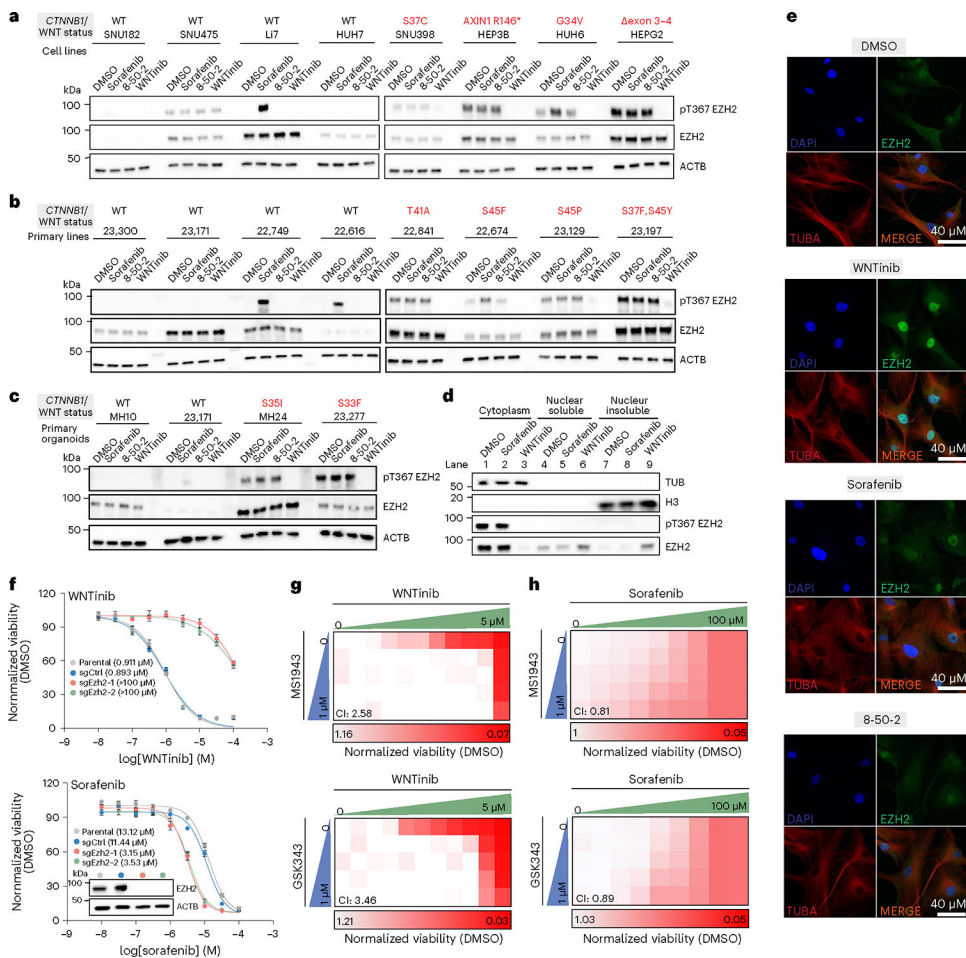
Fig. 3 |. WNTinib depends on EZH2 relocalization to chromatin for its activity in *CTNNB1*-mutated HCC.

a–c, Total and pT367 EZH2 levels in human liver cancer cell lines (**a**; matched to Fig. 1d), primary cell lines (**b**; matched to Fig. 1e) or organoids (**c**; matched to Fig. 1f) either mutated or WT for *CTNNB1*. Models were treated with sorafenib (5 μM), 8–50-2 (1 μM) or WNTinib (1 μM) for 24 h. **d**, Cytoplasmic and nuclear fractions of total and pT367 EZH2 from human HCC primary cell-line 23129 treated with DMSO, sorafenib (5 μM) or WNTinib (1 μM) for 24 h. Tubulin and histone H3 used as fractionation controls**. e**, Immunofluorescence images of EZH2 (green) localization in the human HCC primary cell-line 23129 treated with DMSO, sorafenib (5 μM), 8–50-2 (1 μM) or WNTinib (1 μM) for 24 h. DAPI (blue) was used as a nuclear stain and tubulin (TUBA, red) as a cytoplasmic stain. Scale bar, 40 μm. **f**, IC$_{50}$ curves for WNTinib (top) or sorafenib (bottom) in *MYC-CTNNB1* tumor organoids depleted for EZH2 using CRISPR. Organoids were treated for 3 d. Inset, western blot depicting depletion efficiency ($n = 3$ independent experiments (mean, s.e.m.)). **g,h**, Combination treatment matrices for *MYC-CTNNB1* tumor organoids treated with WNTinib (**g**) or sorafenib (**h**) and compounds targeting EZH2 (top, MS1943 EZH2 degrader; bottom, GSK343 EZH2 SAM competitive inhibitor). Tumor organoids were first treated with MS1943 or GSK343 for 3 d, followed by co-treatment with sorafenib or WNTinib for an additional 3 d ($n = 2$ independent experiments). CI values were

calculated for each column and averaged across each matrix. Western blotting results were independently validated at least twice. For **e**, representative images are shown from $n = 10$ independent images captured from $n = 2$ independent experiments.
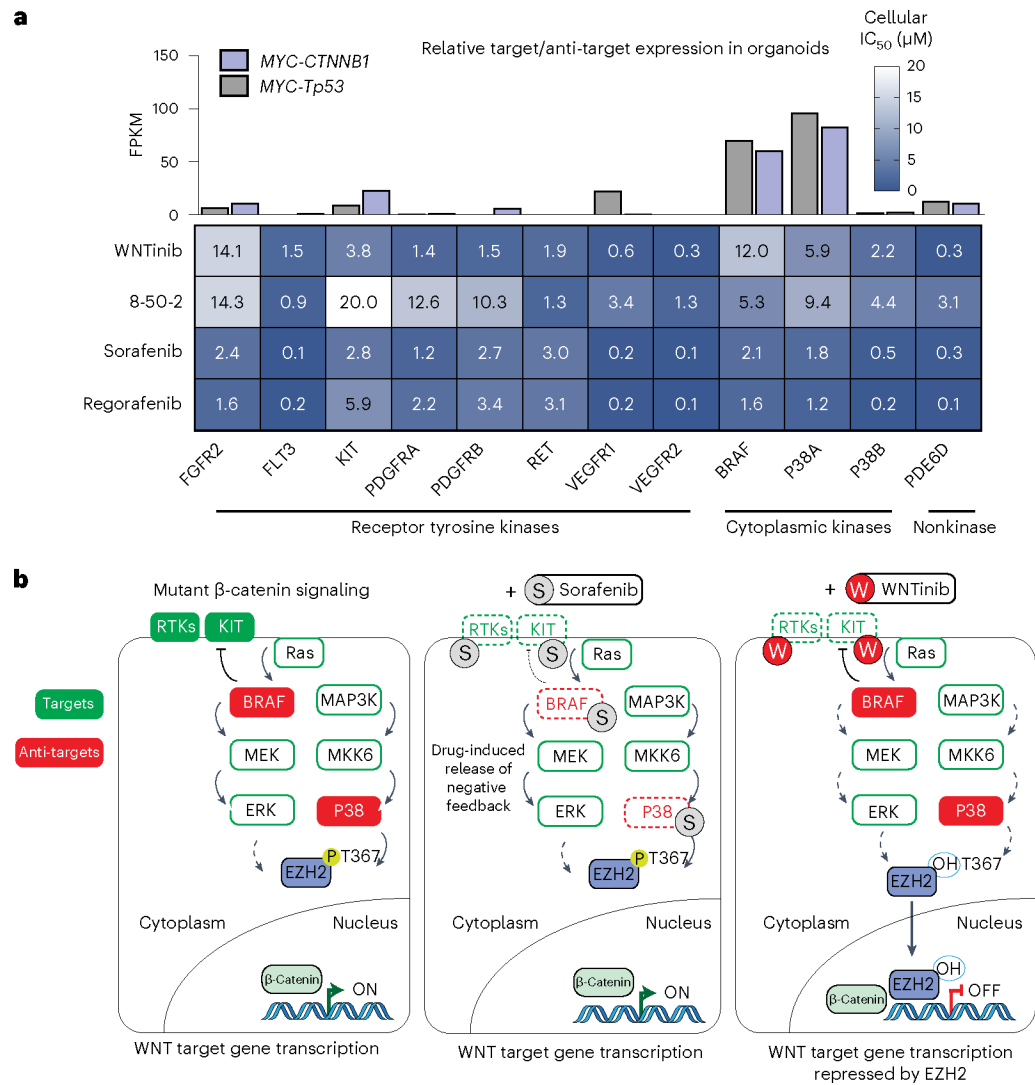
Fig. 4 |. WNTinib utilizes unique polypharmacology to regulate the EZH2–WNT axis.
a, Live-cell target engagement IC_{50} values for sorafenib, regorafenib, 8–50-2 and WNTinib on clinically relevant receptor tyrosine kinases, cytoplasmic kinases and nonkinases. Above, RNA expression of targets in *MYC-CTNNB1* and *MYC-Tp53* tumor organoids. Heatmap displays averages from $n = 3$ independent experiments. FPKM, Fragment per kilobase of transcript per million mapped reads. **b**, Model. Left, phosphorylation of EZH2 is regulated downstream of an RTK KIT signaling axis with negative feedback mediated through cytoplasmic kinases, including BRAF and p38. Middle, sorafenib inhibition on upstream targets is mitigated due to release of negative feedback signaling through direct binding on BRAF and p38. Right, WNTinib strongly downregulates phosphor-EZH2 due to inhibition of targets and removal of anti-target inhibition, thereby avoiding compensatory feedback. As a result, unphosphorylated EZH2 localizes to the nucleus to repress the transcription of WNT targets.
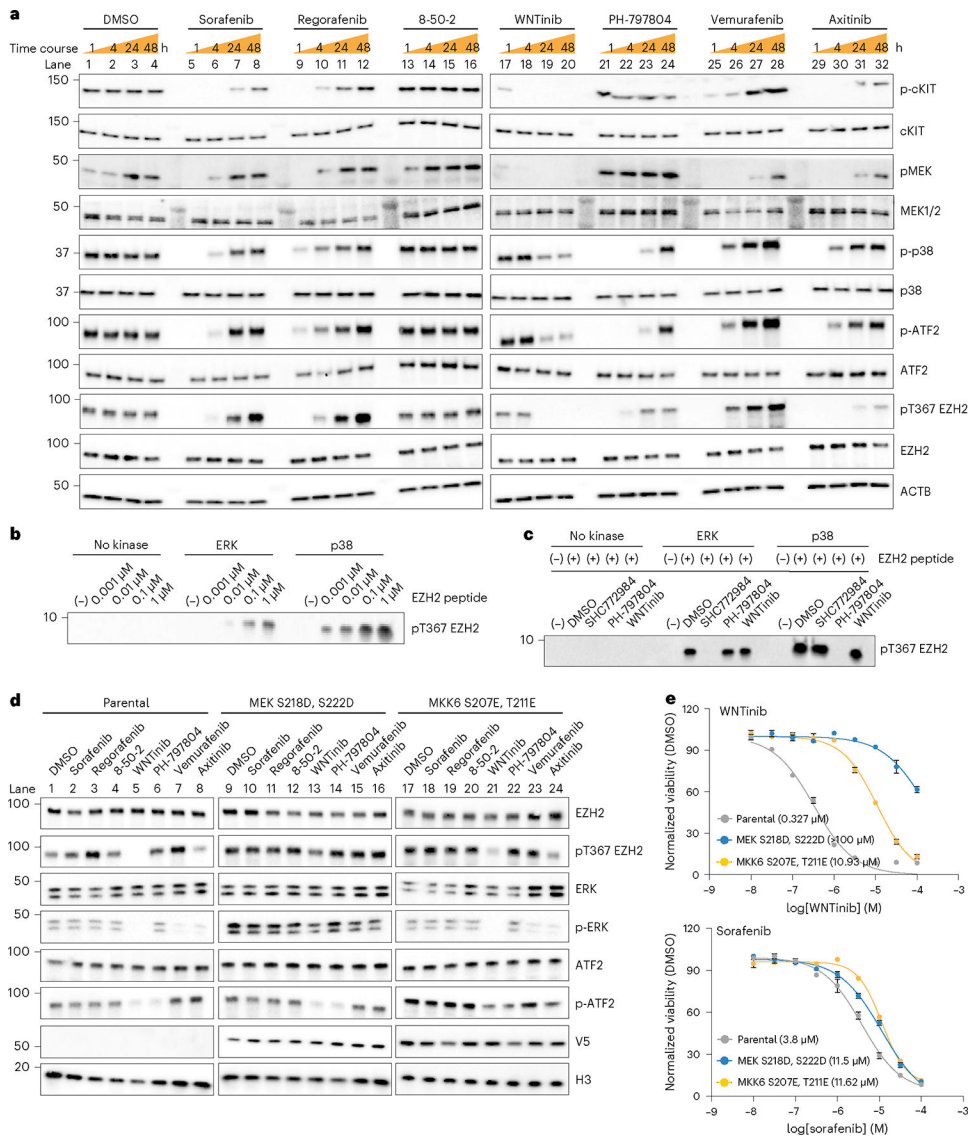
Fig. 5 |. WNTinib utilizes unique polypharmacology to regulate the EZH2–WNT axis.
a, Time course (1–48 h) of signaling perturbations on relevant targets to the model shown in Fig. 4b (p-KIT, pMEK, p-p38, p-ATF2 and pT367 EZH2). *MYC-CTNNB1* tumor organoids were treated with DMSO, sorafenib (10 μM), regorafenib (10 μM), 8–50-2 (1 μM), WNTinib (1 μM), PH-797804 (10 μM), vemurafenib (10 μM) or axitinib (5 μM). Western blotting measures endogenous proteins as indicated. **b**, In vitro kinase assay using either activated ERK or p38 kinases and an EZH2 peptide encoding the T367 site. **c**, In vitro kinase assay conducted as in **b**, but using a set concentration of the EZH2 peptide (1 μM). Relevant inhibitors (SHC772984, PH-797804 or WNTinib; all used at 1 μM) were used to gauge target engagement and concomitant suppression of pT367 EZH2. **d**, Total and pT367 EZH2 levels in HEPG2 cells transduced with constructs encoding constitutively active MEK (Ser218Asp, Ser222Asp) or MKK6 (Ser207Glu, Thr211Glu). Parental HEPG2 cells were used as a control comparison. Cells were treated with DMSO, sorafenib (5 μM), regorafenib (10 μM), 8–50-2 (0.5 μM), WNTinib (0.5 μM), PH-797804 (10 μM), vemurafenib (10

μM) or axitinib (5 μM) for 24 h. The V5 antibody was used to assess overexpression of mutant constructs. **e**, IC_{50} curves for WNTinib (top) or sorafenib (bottom) in HEPG2 cells transduced with constructs encoding constitutively active MEK (Ser218Asp, Ser222Asp) or MKK6 (Ser207Glu, Thr211Glu). Parental HEPG2 cells were used as a control comparison. Cells were treated for 3 d ($n = 3$ independent experiments (mean, s.e.m.)). Western blotting results were independently validated at least twice.
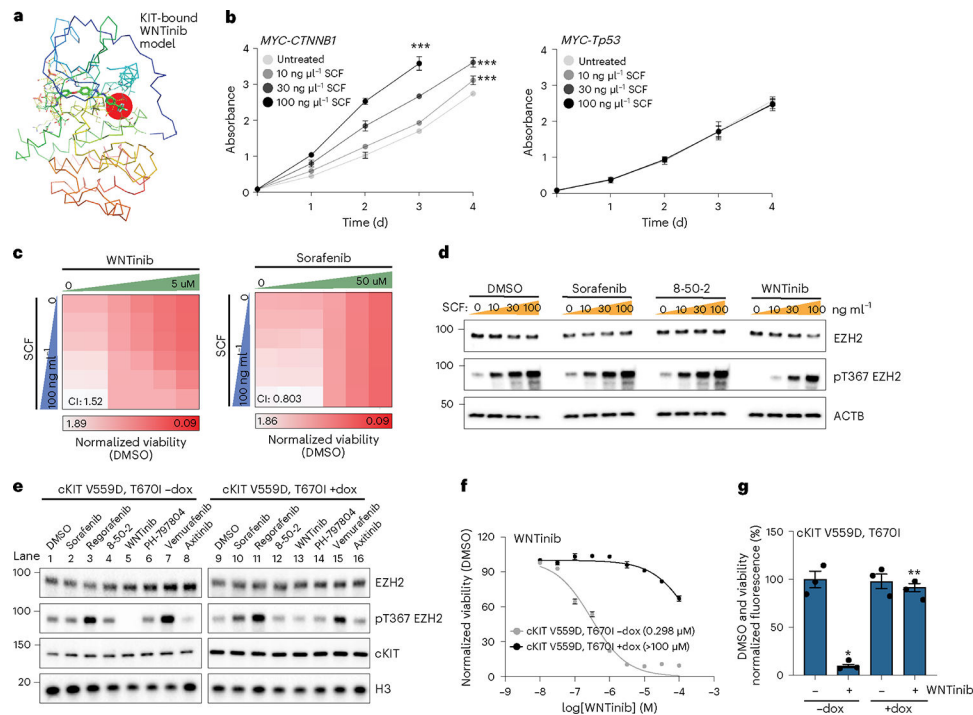
Fig. 6 |. KIT is a critical target for WNTinib's MoA.
a, Model of KIT bound to WNTinib. The inactive type II conformation enables binding through the p-C_2F_5 group, which is highlighted with a red sphere. **b**, Growth curves for *MYC-CTNNB1* tumor organoids (left) or *MYC-Tp53* tumor organoids (right) treated with increasing doses of cKIT ligand/SCF (n = 3 independent experiments (mean, s.e.m.)). Significant differences between curves (compared with untreated) are indicated by asterisks: ***P < 0.0005, as calculated using a two-way ANOVA and Tukey's test for multiple comparisons ($F_{[4, 20]}$ = 7.1). **c**, Combination treatment matrices for *MYC-CTNNB1* tumor organoids treated with WNTinib (left) or sorafenib (right) and SCF. Tumor organoids were treated for 3 d (n = 2 independent experiments). CI values were calculated for each column and averaged across each matrix. **d**, Western blot depicting the modulation of pT367 EZH2 by increasing titration of SCF in *MYC-CTNNB1* tumor organoids treated with sorafenib (10 μM), 8–50-2 (1 μM) or WNTinib (1 μM) for 24 h. **e**, Total and pT367 EZH2 levels in HEPG2 cells transduced with a doxycycline (dox)-inducible construct encoding constitutively active cKIT (Val559Asp, Thr670Ile). Cells were treated with DMSO, sorafenib (5 μM), regorafenib (10 μM), 8–50-2 (0.5 μM), WNTinib (0.5 μM), PH-797804 (10 μM), vemurafenib (10 μM) or axitinib (5 μM) for 24 h. **f**, IC_{50} curve for WNTinib in HEPG2 cells transduced as in **e**. Doxycycline-untreated HEPG2 cells were used as a control comparison. Cells were treated for 3 d (n = 3 independent experiments (mean, s.e.m.)). **g**, WNT reporter expression levels in HEPG2 cells transduced with the cKIT-V559D, T670I construct and treated with WNTinib (0.5 μM) for 24 h (n = 3 independent experiments (mean, s.e.m.)). Significant differences between groups are indicated by asterisks.: *P < 0.05, **P < 0.005 as calculated using two-tailed, paired Student's t-tests. For **b**, left: P values: ***P < 0.0001 (10, 30 and 100 ng μl^{-1} of SCF). For **g**,

P values: *P = 0.009 (−dox, +WNTinib), **P = 0.0012 (+dox, +WNTinib). Western blotting results were independently validated at least twice.
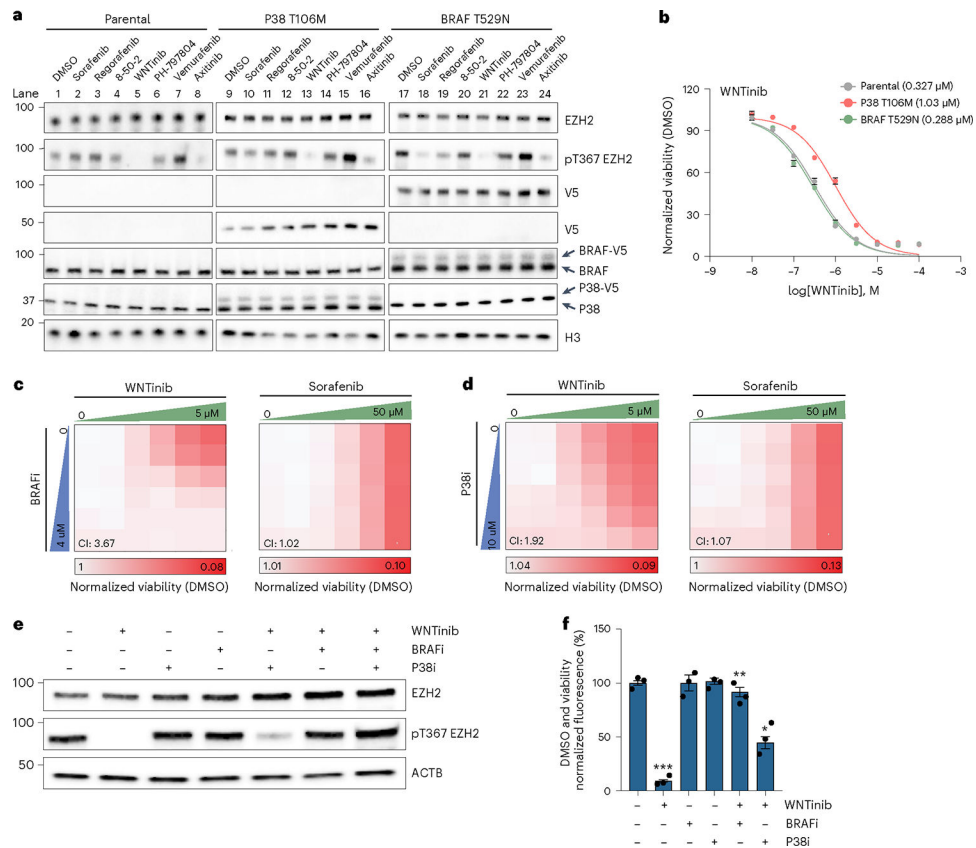
Fig. 7 |. BRAF and p38 kinases are critical anti-targets for WNTinib.

a, Total and pT367 EZH2 levels in HEPG2 cells transduced with constructs encoding drug-resistant p38 (Thr106Met) or BRAF (Thr529Asn) kinases. Parental HEPG2 cells were used as control comparison. Cells were treated with DMSO, sorafenib (5 μM), regorafenib (10 μM), 8–50-2 (0.5 μM), WNTinib (0.5 μM), PH-797804 (10 μM), vemurafenib (10 μM) or axitinib (5 μM) for 24 h. V5 and endogenous antibodies were used to assess overexpression of mutant constructs. **b**, IC$_{50}$ curve for WNTinib in HEPG2 cells transduced with constructs encoding drug-resistant p38 (Thr106Met) or BRAF (Thr529Asn) kinases. Parental HEPG2 cells were used as a control comparison. Cells were treated for 3 d ($n = 3$ independent experiments (mean, s.e.m.)). **c,d**, Combination treatment matrices for *MYC-CTNNB1* tumor organoids treated with WNTinib (left) or sorafenib (right) and the BRAF inhibitor dabrafenib (**c**) or the p38 inhibitor SB202190 (**d**). Tumor organoids were treated for 3 d ($n = 2$ independent experiments). CI values were calculated for each column and averaged across each matrix. **e**, Western blot depicting the modulation of pT367 EZH2 by WNTinib (1 μM) alone or in combination with dabrafenib (10 μM), SB202190 (10 μM) or the two compounds together. *MYC-CTNNB1* tumor organoids were treated for 24 h. **f**, WNT reporter expression levels in *MYC-CTNNB1* tumor organoids treated with WNTinib alone (1 μM) or in combination with dabrafenib (10 μM) or SB202190 (10 μM) for 24 h ($n = 3$ independent experiments (mean, s.e.m.)). Significant differences between groups are indicated by asterisks: *$P < 0.05$, **$P < 0.005$, ***$P < 0.0005$, as calculated using two-tailed, paired Student's *t*-tests: ***$P = 0.00039$ (WNTinib), **$P = 0.0036$ (WNTinib + BRAFi),

*P = 0.0168 (WNTinib + P38i). Western blot results were independently validated at least twice.
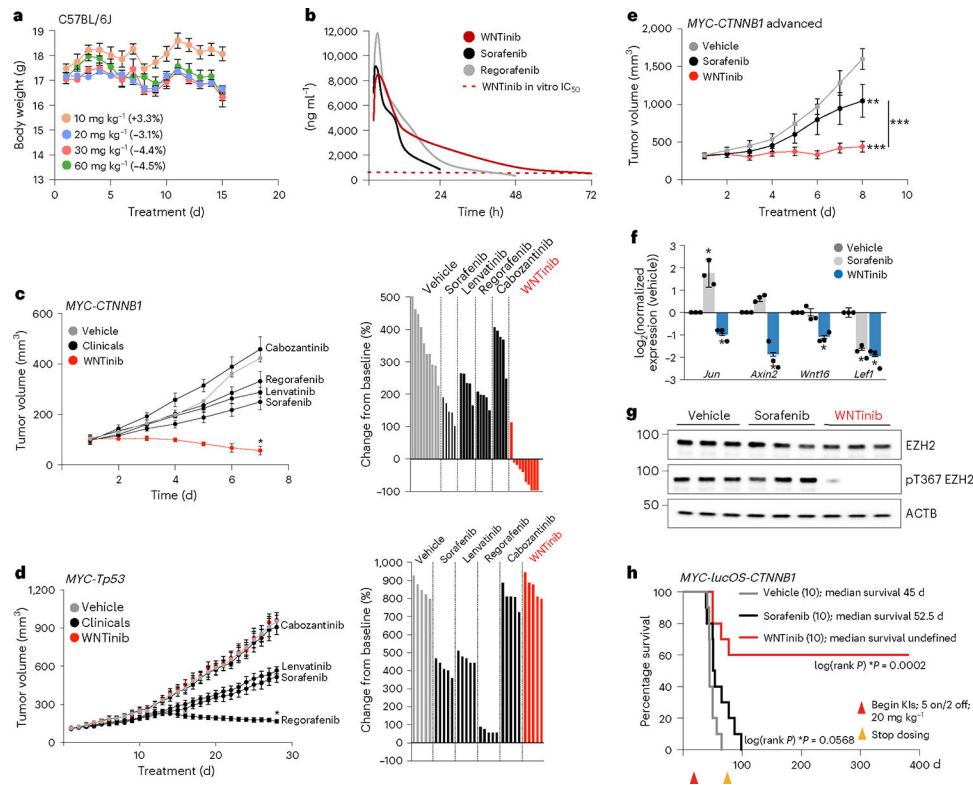
Fig. 8 |. WNTinib outperforms clinical compounds across in vivo models of HCC.

a, Dose escalation of WNTinib in C57BL/6J mice. The percentage change in body weight was noted in brackets ($n = 3$ animals per group (mean, s.e.m.)). **b**, Pharmacokinetic curves of WNTinib, sorafenib and regorafenib in BALB/c animals. For reference, WNTinib's in vitro IC_{50} (1 μM) was denoted with a dashed line. **c**, Left, tumor volume plot in *MYC-CTNNB1* tumor organoid allografts treated with WNTinib or clinical compounds ($n = 10$ animals per group for WNTinib and vehicle; $n = 5$ animals per group for clinicals (mean, s.e.m.)). Right, waterfall plot. Significant differences between groups are indicated by asterisks: *$P < 0.05$, as calculated using a two-way ANOVA with Tukey's test for multiple comparisons ($F[5,36] = 3.349$). **d**, As in **c**, but using *MYC*-Tp53 tumor organoid allografts ($n = 5$ animals per group (mean, s.e.m.)). Significant differences between groups are indicated by asterisks: *$P < 0.05$, as calculated using a two-way ANOVA with Tukey's test for multiple comparisons ($F[5, 36] = 3.485$). For **c** and **d**, the animals were dosed via daily oral gavage using 30 mg kg^{-1} of the respective compounds. **e**, Tumor volume plot in *MYC-CTNNB1* tumor organoid allografts treated with WNTinib or sorafenib ($n = 9$ vehicle; $n = 10$ sorafenib; $n = 11$ WNTinib (mean, s.e.m.)). Significant differences between groups are indicated by asterisks: **$P < 0.005$, ***$P < 0.0005$, as calculated using a two-way ANOVA with Tukey's test for multiple comparisons ($F[4,216] = 4.272$). **f**, The qPCR expression of WNT-target genes in tumors derived from mice in **e** ($n = 3$ per group). *$P < 0.05$, as calculated using two-tailed, paired Student's *t*-tests. **g**, Western blot of pT367 EZH2 in tumors derived from mice in **e** ($n = 3$ per group). **h**, Hydrodynamic tail-vein model of C*TNNB1*-mutated HCC (*MYC*-lucOS; *CTNNB1*) treated with vehicle, sorafenib or WNTinib. Percentage survival is shown and log(rank *P*) values are indicated (compared

with vehicle). Kinase inhibitors were started 7 d post-injection and dosed at 20 mg kg^{-1} (WNTinib) or 30 mg kg^{-1} (sorafenib)—5 d on and 2 d off. Exact P values are listed in Source data.